



**HAL**  
open science

## **A modeling study of processes controlling the Bay of Bengal sea surface salinity interannual variability**

Valiya Parambil Akhil, Matthieu Lengaigne, Jérôme Vialard, Fabien Durand, Madhavan Girijakumari Keerthi, Akurathi Venkata Sai Chaitanya, Fabrice Papa, Vissa Venkata Gopalakrishna, Clément de Boyer Montégut

► **To cite this version:**

Valiya Parambil Akhil, Matthieu Lengaigne, Jérôme Vialard, Fabien Durand, Madhavan Girijakumari Keerthi, et al.. A modeling study of processes controlling the Bay of Bengal sea surface salinity interannual variability. *Journal of Geophysical Research. Oceans*, 2016, 121 (12), pp.8471 - 8495. 10.1002/2016JC011662 . hal-01497558

**HAL Id: hal-01497558**

**<https://hal.science/hal-01497558>**

Submitted on 10 Sep 2021

**HAL** is a multi-disciplinary open access archive for the deposit and dissemination of scientific research documents, whether they are published or not. The documents may come from teaching and research institutions in France or abroad, or from public or private research centers.

L'archive ouverte pluridisciplinaire **HAL**, est destinée au dépôt et à la diffusion de documents scientifiques de niveau recherche, publiés ou non, émanant des établissements d'enseignement et de recherche français ou étrangers, des laboratoires publics ou privés.

Copyright

## RESEARCH ARTICLE

10.1002/2016JC011662

## A modeling study of processes controlling the Bay of Bengal sea surface salinity interannual variability

V. P. Akhil<sup>1,2</sup>, M. Lengaigne<sup>3,4</sup>, J. Vialard<sup>4</sup>, F. Durand<sup>1</sup>, M. G. Keerthi<sup>2</sup>, A. V. S. Chaitanya<sup>2</sup>, F. Papa<sup>1,3</sup>, V. V. Gopalakrishna<sup>2</sup>, and Clément de Boyer Montégut<sup>5</sup><sup>1</sup>LEGOS, Université de Toulouse, IRD, CNES, CNRS, UPS, Toulouse, France, <sup>2</sup>NIO, Goa, India, <sup>3</sup>Indo-French Cell for Water Sciences, IISc-NIO-IITM-IRD Joint International Laboratory, NIO, Goa, India, <sup>4</sup>LOCEAN-IPSL, Sorbonne Universités, UPMC, Univ Paris 06, -CNRS-IRD-MNHN, Paris, France, <sup>5</sup>LOPS, IFREMER, Plouzané, France

## Key Points:

- Largest SSS variability occurs along the northern and western Bay
- In northern BoB SSS, variability is mostly driven by the GB runoff interannual variations
- IOD drives SSS variability of opposite polarity along the western Bay and Southern Andaman Sea

## Correspondence to:

V. P. Akhil,  
akhil1585@gmail.com

## Citation:

Akhil, V. P., M. Lengaigne, J. Vialard, F. Durand, M. G. Keerthi, A. V. S. Chaitanya, F. Papa, V. V. Gopalakrishna, and C. de Boyer Montégut (2016), A modeling study of processes controlling the Bay of Bengal sea surface salinity interannual variability, *J. Geophys. Res. Oceans*, 121, 8471–8495, doi:10.1002/2016JC011662.

Received 19 JAN 2016

Accepted 31 OCT 2016

Accepted article online 7 NOV 2016

Published online 7 DEC 2016

**Abstract** Recent observational studies provided preliminary insights on the interannual variability of Bay of Bengal (BoB) Sea Surface Salinity (SSS), but are limited by the poor data coverage. Here, we describe the BoB interannual SSS variability and its driving processes from a regional eddy-permitting ocean general circulation model forced by interannually varying air-sea fluxes and altimeter-derived discharges of major rivers over the past two decades. Simulated interannual SSS variations compare favorably with both in situ and satellite data and are largest in boreal fall in three regions: the northern BoB, the coastal region off east India, and the Andaman Sea. In the northern BoB, these variations are independent from those in other regions and mostly driven by summer-fall Ganga-Brahmaputra runoff interannual variations. In fall, remote forcing from the Indian Ocean Dipole results in anticlockwise anomalous horizontal currents that drive interannual SSS variations of opposite polarity along the east coast of India and in the Southern Andaman Sea. From winter onward, these anomalies are damped by vertical mixing in the northern BoB and along the east coast of India and by horizontal advection in the Southern Andaman Sea. While river runoff fluctuations locally play a strong role near the Ganga-Brahmaputra river mouth, wind-driven interannual current anomalies are responsible for a large fraction of SSS interannual variability in most of the basin.

## 1. Introduction

The Bay of Bengal (BoB) is a semienclosed tropical basin, landlocked by the Asian continent to the north. This basin is forced by annually reversing monsoonal winds that blow from the southwest during the summer monsoon (May–September) and from the northeast during the winter monsoon (November–March). Those alternating winds drive a well-defined, seasonally reversing western boundary current in the BoB, the East Indian Coastal Current (EICC). The EICC flows northward before the summer monsoon and southward right after [Shankar *et al.*, 1996; McCreary *et al.*, 1996] and is largely responsible for the exchange of water masses between the BoB and Arabian Sea [Shetye *et al.*, 1996; Durand *et al.*, 2007 and references therein]. The BoB is also characterized by a large seasonal freshwater influx from rivers as well as excess precipitation over evaporation [Shenoi *et al.*, 2002]. A large fraction of this net freshwater flux to the ocean occurs during or shortly after the monsoon, with a similar contribution from continental runoffs and monsoonal oceanic rainfall over the northern half of the BoB [e.g., Chaitanya *et al.*, 2014]. The largest rivers that flow into the BoB are the Ganga-Brahmaputra (GB) in the northern end of the BoB and the Irrawaddy along the eastern side, with an average discharge of  $\sim 8.7 \times 10^4 \text{ m}^3 \text{ s}^{-1}$  and  $\sim 3.4 \times 10^4 \text{ m}^3 \text{ s}^{-1}$ , respectively, during July–September [Papa *et al.*, 2012; Dai and Trenberth, 2002]. Three smaller rivers on the East Indian coast (Mahanadi, Godavari, and Krishna) contribute to  $\sim 10^4 \text{ m}^3 \text{ s}^{-1}$  together. As a result of this intense freshwater flux in a semienclosed and relatively small basin, the BoB stands out as a very peculiar region for salinity distribution in the tropical belt, with sea surface salinity (SSS) as low as 28 pss in the northern part of the Bay. These low-salinity surface waters lay above much saltier subsurface waters, resulting in a sharp near-surface haline stratification [Shetye, 1993; Vinayachandran *et al.*, 2013].

This intense near-surface haline stratification has been suggested to promote a positive feedback that allows maintaining intense convective rainfall over the BoB [Shenoi *et al.*, 2002]. These surface fresh waters strengthen the density stratification and maintain a thin mixed layer [Mignot *et al.*, 2007; Thadathil *et al.*, 2007; Girishkumar *et al.*, 2013]. Combined with a homogeneous thermal stratification, this often results in

the formation of a barrier layer [Lukas and Lindstrom, 1991], an isothermal and salinity-stratified layer below the surface mixed layer. This barrier layer prevents turbulent entrainment of cooler thermocline water into the mixed layer [de Boyer Montégut et al., 2007] and has hence been suggested to maintain sea surface temperature (SST) above 28°C [Shenoi et al., 2002], a necessary condition for deep atmospheric convection [Gadgil et al., 1984]. The salinity stratification also contributes to weaken the oceanic cooling under tropical cyclones after the monsoon [e.g., Neetu et al., 2012], hence potentially favoring intense cyclones [Sengupta et al., 2008]. These strong impacts of haline stratification in the BoB call for a better description and understanding of the SSS spatial and temporal variability within the Bay.

Several studies have already investigated the BoB seasonal SSS variations, using both observations [Rao and Sivakumar, 2003; Shetye, 1993; Shetye et al., 1991, 1996; Vinayachandran et al., 2002; Vinayachandran and Kurian, 2007; Chaitanya et al., 2014] and models [Jensen, 2001; Benshila et al., 2014; Akhil et al., 2014]. They all reported a marked SSS seasonal cycle, especially in the northern part of the basin. From summer to fall, a large pool of fresh surface waters develops in the northern part of the basin. This fresh pool then spreads southward along both eastern and western boundaries of the basin in fall and early winter. These fresh waters start retreating back northward in winter, to reach their minimal extent in spring. Previous studies [Shetye et al., 1996; Han et al., 2001; Sengupta et al., 2006; Akhil et al., 2014] showed that the strong freshening during the monsoon mostly results from the GB river discharge. The southward expansion of fresh water along the east coast of India in fall has been further attributed to horizontal advection of fresh waters from the northern BoB by the southward-flowing EICC [Shetye et al., 1996; Chaitanya et al., 2014; Akhil et al., 2014; Benshila et al., 2014]. Recent observations [Chaitanya et al., 2014; Hareesh Kumar et al., 2013] and historical cruise data [Shetye et al., 1996] indicate that the seasonal freshening along the East Indian coast occurs in a narrow (~100 km wide) band with coastal waters up to 10 pss fresher than those offshore, a feature that has been dubbed “the river in the sea” [Chaitanya et al. 2014]. While the southward expansion of this “river in the sea” is attributed to horizontal advection by the EICC, its erosion occurs prominently through vertical exchanges of salt at the bottom of the mixed layer [Akhil et al., 2014].

Although the seasonal cycle is by far the most energetic timescale of upper BoB variability, the BoB climate also exhibits clear interannual variations. The patterns of precipitation over the BoB and adjoining continents [e.g., Gadgil, 2003] and the related riverine freshwater supply to the BoB [Papa et al., 2012] indeed vary significantly from year to year. Three main climatic modes influence the interannual variability of wind and precipitation over the tropical Indian Ocean: the El Niño-Southern Oscillation (ENSO), the Indian Ocean Dipole (IOD), and the interannual fluctuations of the summer monsoon. ENSO originates in the tropical Pacific but remotely impacts the Indian Ocean by inducing anomalous subsidence there, resulting in a general warming of the basin [e.g., Klein et al., 1999; Xie et al., 2009]. The IOD is an indigenous mode of interannual variability of the Indian Ocean [Saji et al., 1999; Webster et al., 1999], which often (but not always) cooccurs with ENSO [e.g., Yamagata et al., 2004; Izumo et al., 2014]. Peaking in boreal fall, it has a shorter lifetime than ENSO events, about 6 months. It is associated with a well-defined cold anomaly along the coast of Java and Sumatra, and more variable warming of the western part of the basin. The cooling off Java and Sumatra is associated with a local suppression of convection there, which is associated with anomalous easterlies over the central Indian Ocean. Finally, interannual fluctuations of the Indian summer monsoon drive strong interannual wind, precipitation, and runoffs anomalies over the northern Indian Ocean [Gadgil, 2003]. ENSO partly drives these interannual fluctuations of the summer monsoon through atmospheric teleconnections [Vecchi and Harrison, 2004; Mujumdar et al., 2012], in particular with a tendency toward rainfall deficit over the Ganges-Mahanadi watershed during El Niño years.

Several studies [Shankar, 1998; Rao et al., 2002; Thompson et al., 2006; Jensen, 2007] demonstrated that a positive IOD induces a negative sea level anomaly (SLA) along the rim of the Bay in fall, resulting in an anomalous cyclonic circulation in the BoB. Negative SLAs have also been reported off the east coast of India during El Niño events [Han and Webster, 2002; Srinivas et al., 2005; Singh, 2002]. However, due to the cooccurrence of ENSO with IOD events, these studies did not clearly distinguish the respective impact of these two modes on SLA in the BoB. Aparna et al. [2012] addressed this issue and showed that these two modes have distinct SLA signatures, IOD events being associated with a single SLA peak in fall along the rim of the Bay while ENSO exhibits weaker but multiple SLA peaks (April–December and November–July), with a relaxation between the two peaks.

The scarcity of available SSS in situ observations and the lack of reliable continental freshwater fluxes did for long prevent the monitoring of the BoB SSS interannual variability (hereafter IAV). The improvement of the SSS observing system through the advent of the Argo program and the new dataset of satellite altimeter-derived discharges of major rivers that flow into the Bay [Papa *et al.*, 2012] recently allowed to provide a qualitative description of the year-to-year SSS variability over the BoB [Chaitanya *et al.*, 2014; Pant *et al.*, 2015]. These studies reported, in particular, a strong SSS IAV in the northern BoB. Pant *et al.* [2015] highlighted fresh salinity anomalies in this region from June to February for three specific years over the 2006–2012 period and attributed these anomalous events to positive IOD events. Based on a simple mixed-layer model salt budget, both Chaitanya *et al.* [2014] and Pant *et al.* [2015] concluded that SSS IAV is mainly driven by fresh water fluxes in the northern BoB during summer season. The analysis of Pant *et al.* [2015] further suggested that this anomalous summer freshening is driven by enhanced precipitation associated with positive IODs and that it is further advected southward by the anticyclonic circulation pattern associated with the onset of the winter monsoon.

On the modeling front, there are only a handful of studies that discussed SSS IAV in the BoB. Forced ocean model studies suggested that the anomalous clockwise BoB circulation associated with positive IOD events induce fresh SSS anomalies in the eastern part of the Bay through anomalous advection of climatological basin-scale zonal SSS gradient [Thompson *et al.*, 2006; Grunseich *et al.*, 2011]. Using coupled model outputs, Vinayachandran and Nanjundiah [2009] suggested that, along with the equatorial Indian Ocean, the northern BoB in summer exhibits the largest SSS IAV, and that this variability is largely driven by year-to-year variations in the monsoonal fresh water flux. They also underline the role of anomalous alongshore advection in driving the SSS IAV along the east coast of India during the summer monsoon but the unrealistic runoff and oceanic precipitation forcing generated by their coupled model considerably hampers the robustness of their results. By forcing an ocean model with interannually varying discharges of the GB river system, Durand *et al.* [2011] demonstrated the large impact of these rivers on SSS IAV north of 15°N. The above studies therefore suggested that SSS IAV in the BoB is rather large, with a considerable influence of GB river runoff and precipitations at the head of the Bay.

Past studies of the BoB SSS IAV have, however, underlined some limitations. The limited observational coverage for example hampers the knowledge of patterns of observed SSS variability, while observationally derived salt budgets do not allow estimating explicitly the contribution from vertical processes (mixing, upwelling) and are affected by observational errors, in particular on the mixed layer depth estimates. In addition, an accurate estimate of major river runoffs interannual variations in the Bay of Bengal, an essential input for modeling SSS IAV in this basin, only became recently available [Papa *et al.* 2012]. No modeling study did so far provide a quantitative estimate of the respective influence of wind-driven circulation, rainfall, and rivers runoff anomalies on the BoB SSS IAV. This therefore calls for a more detailed study using an ocean circulation model to revisit the conclusions of the above studies in a more sophisticated numerical framework.

The goal of the present study is therefore to fill that gap by using an ocean model forced by interannual winds, precipitation, and river runoffs from all major rivers that flow into the BoB. The paper is organized as follows. In section 2, we describe the reference simulation and sensitivity experiments, the mixed layer salinity budget, the validation data sets, as well as the statistical methods used to infer the respective influence of each process on the SSS IAV in the Bay. Section 3 provides a validation of SSS IAV in our reference experiment. A detailed description of the main modes of SSS IAV in the Bay from the reference experiment and their relationships with the main interannual modes of climate variability is further provided in section 4. This section also assesses the mechanisms driving these variations through the analysis of sensitivity experiments forced either by interannual runoffs, oceanic precipitation, or wind stress and through analysis of mixed layer salinity budget. The last section summarizes and discusses the outcome of the present study.

## 2. Data and Methods

### 2.1. Model Configuration and Forcing

The model configuration used in this study is based on the Nucleus of European Modeling of Ocean (NEMO) ocean general circulation modeling system [Madec, 2008], implemented in a regional Indian Ocean configuration (27°E–142°E, 33°S–30°N) described in Vialard *et al.* [2013] and Akhil *et al.* [2014]. It solves the

primitive equations on a  $1/4^\circ$  horizontal grid with 46 vertical levels (vertical resolution ranging from 6 m at the surface to 250 m at the bottom, with seven levels in the upper 50 m). Vertical mixing is parameterized using a turbulent closure scheme that resolves a prognostic equation for the turbulent kinetic energy [Blanke and Delecluse, 1993]. The open boundaries are handled using a radiation-relaxation approach [Marchesiello et al., 2001], where radiation conditions are used to determine whether a boundary is passive (outward propagation) or active (inward propagation). The boundaries are constrained with a 150 day time-scale relaxation to 5 day average velocities, temperature, and salinity from an interannual global  $1/4^\circ$  simulation [see Nidheesh et al., 2012; Keerthi et al., 2013], which has been carried out in the framework of the Drakkar project [Drakkar Group, 2007].

The simulations analyzed in the present paper are obtained using a model configuration and forcing strategy similar to those used in Akhil et al. [2014], the only differences being the forcing fields and the duration of experiments. The model computes the latent heat, sensible heat, upward longwave radiation, and shortwave radiation fluxes using bulk formulae. Most of the input atmospheric variables (near surface wind, air temperature, and specific humidity, downward longwave fluxes) used for the simulations in this study are from DFS5.2 described in Brodeau et al. [2012] and Dussin et al. [2014]. DFS5.2 is derived from ERA40 [Uppala et al., 2005] until 2002 and ERA-Interim reanalysis [Dee et al., 2011] afterward. The Daily TropFlux  $1^\circ \times 1^\circ$  gridded product [Praveen Kumar et al., 2012] provides downward short wave radiation, derived from the (ISCCP)-FD surface radiations [Zhang et al., 2004] with ad hoc corrections derived from the tropical moored buoy array.

The model is forced with interannually varying precipitations from the GPCP product [Huffman et al., 1997], while evaporation is computed interactively using bulk formulae and prescribed air relative humidity and winds from the DFS5.2 data set. We use the interannually varying monthly estimates of the GB runoff described in Papa et al. [2012]. This time-series is derived from a combination of in situ level-discharge relationships, the so-called rating curve [Papa et al., 2010], with river water level retrieved from multiple satellite altimeters (TOPEX/Poseidon, ERS-2, ENVISAT, and Jason-2). For the Irrawaddy river, in situ discharge time series are unfortunately not available over the recent period. Furuichi et al. [2009] published monthly estimates derived from in situ observations over the 1966–1996 period. Following a similar approach to that of Papa et al. [2012], we used these monthly in situ discharge estimates, together with TOPEX/Poseidon river level time series over their common period of availability (1993–1996) to determine a rating curve. We then used this rating curve to derive a continuous, monthly estimate of the Irrawaddy river discharge at the river mouth for 1993–2012 using TOPEX/Poseidon (1993–2002), ENVISAT (2002–2008), and Jason-2 (2008 onward). For the peninsular rivers flowing along the east coast of India (Mahanadi, Godavari, Krishna; hereafter PNR), we use interannual gauge discharge data (<http://www.india-wris.nrs.gov.in/>). The yearly average discharge from each of these rivers flowing into the Bay is scaled by a constant coefficient to constrain the long-term mean discharge to be identical to that of Dai and Trenberth [2002]. All other rivers discharges injected into the model are based on the monthly climatology of Dai and Trenberth [2002]. No relaxation to observed SSS climatology is applied in any of the simulations used in this study.

Figure 1 allows discussing the amplitude and patterns of interannual variability of the air-sea fluxes contributing to the modeled SSS IAV for each season, i.e., precipitation, runoffs, and wind speed (that ultimately affects the salinity by modulating the oceanic circulation and vertical mixing). In the northern BoB, both freshwater forcing and winds exhibit a maximum interannual variability during and/or shortly after the monsoon (in JJA and SON). The GB river system (red dots on Figure 1) and the peninsular rivers (Mahanadi, Godavari, Krishna; blue stars) exhibit maximum variations during the postmonsoon season (SON) with interannual standard deviations of 1.40 and 0.75 mm/d, respectively. Maximum interannual variations of the Irrawaddy river discharge (green dots) occur earlier, i.e., during the summer monsoon (0.96 mm/d in JJA), when GB river discharge displays similar amplitude of variations (0.91 mm/d). During winter (DJF) and spring (MAM), interannual runoffs variations of these major rivers are about one order of magnitude weaker than those during and shortly after the monsoon. Precipitation displays maximum interannual variability in the northeastern part of the basin during and shortly after the summer monsoon (Figures 1a and 1b). When averaged over the oceanic region north of  $14^\circ\text{N}$ , the amplitude of this interannual variability amounts to 1.05 mm/d in JJA and 1.1 mm/d in SON, an amplitude similar to that of major river runoffs. The precipitation interannual variability in the northern part of the Bay considerably weakens in winter and spring (Figures 1c and 1d), with a maximum of variability located in southern BoB east of Sri Lanka during the winter monsoon

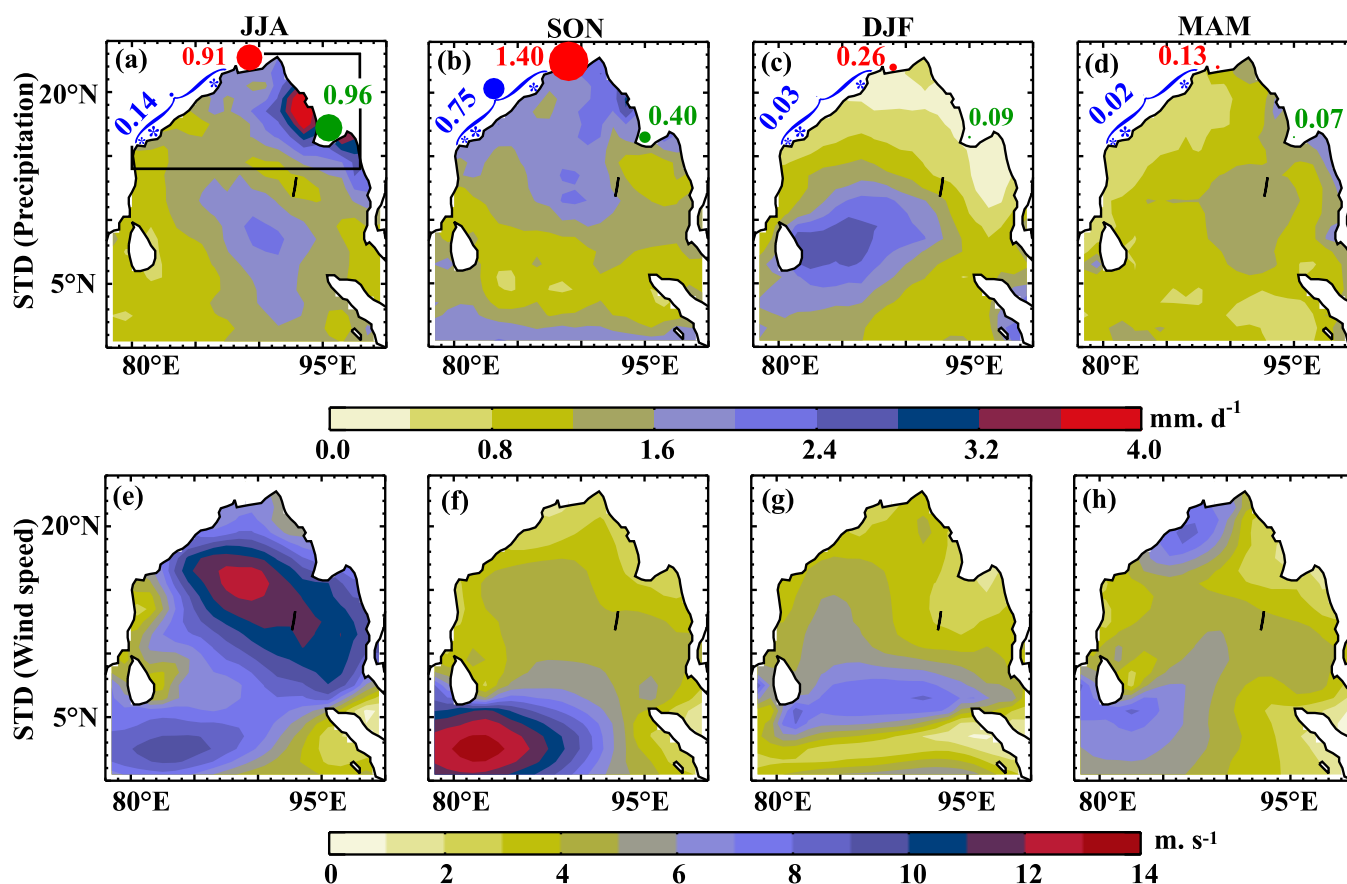


**Figure 1.** Standard deviation of (first row) interannual precipitation anomalies and (second row) wind speed anomalies, for June–August (JJA), September–November (SON), December–February (DJF), and March–May (MAM). The dots on first row indicate the location of the mouth of all major rivers: the Ganga-Brahmaputra (red), Irrawady (green), and peninsular rivers (total of Mahanadi, Godavari, Krishna; blue). The radius of each dot is proportional to the standard deviation of the runoff interannual anomaly, with the value (in  $\text{mm.d}^{-1}$ ) indicated close to each dot. The river runoffs (volume per unit of time) were converted into an equivalent height per unit of time ( $\text{mm.d}^{-1}$ ) through a division by the oceanic area situated northward of  $14^\circ\text{N}$  (oceanic surface of the black box on panel (a)).

(Figure 1c). The amplitude of interannual wind variability is maximum in the central BoB during summer monsoon and south of Sri Lanka in the equatorial region during fall, a variability that is largely related to the IOD [e.g., *Saji and Yamagata*, 2003]. To summarize, this figure clearly illustrates that both freshwater flux and wind forcing in the northern BoB exhibit a maximum variability during and shortly after the summer monsoon, with considerably less variations during the following seasons.

## 2.2. Reference and Sensitivity Experiments

Using the aforementioned model configuration and forcing, a reference experiment (hereafter REF) initialized at rest from the World Ocean Atlas temperature and salinity climatologies [*Locarnini et al.*, 2010] is performed over the 1990–2012 period. This experiment is analyzed over the 1993–2012 period to allow the ocean to spin-up over the first 3 years of the experiment. Experiments using this model configuration and a similar forcing strategy have been shown to successfully reproduce the seasonal SSS variability in the BoB [*Akhil et al.*, 2014] as well as the variability over the Indian Ocean at a wide range of timescales [*Nisha et al.*, 2013; *Vialard et al.*, 2013; *Keerthi et al.*, 2013; *Praveen Kumar et al.*, 2014; *Keerthi et al.*, 2016].

In order to assess the mechanisms at stake in driving SSS IAV in the reference experiment, a series of sensitivity experiments is also performed using interannually varying fluxes either from runoffs, precipitations, or wind stress, but prescribing the seasonal climatology of the two remaining fluxes. Table 1 summarizes the experiments used in this study: the  $\text{Tau}_{\text{int}}$  experiment is forced by interannual wind stress forcing, but uses a seasonal climatology of fresh water fluxes (precipitation and runoffs). The  $\text{P}_{\text{int}}$  experiment is forced by interannual precipitation but uses a seasonal climatology of wind stress and river runoffs. Finally, the  $\text{R}_{\text{int}}$  experiment uses interannual runoffs, keeping precipitation and wind stress forcing to climatological values.

**Table 1.** List of Experiments Used in This Study

Name	Description
REF	Interannual forcing (all fluxes)
Tau <sub>int</sub>	Wind stress: interannual/precipitation and runoff: climatological
P <sub>int</sub>	Precipitation: interannual/wind stress and runoff: climatological
R <sub>int</sub>	River runoff: interannual/wind stress and precipitation: climatological

All sensitivity experiments are run over the 1990–2012 period, from the same initial condition as REF and are analyzed over the 1993–2012 period. Interannual anomalies are calculated by removing the model mean seasonal cycle over the 1993–2012 period.

The comparison between SSS interannual anomalies (hereafter SSS') simulated by REF and each sensitivity experiment allows an estimation of the SSS' signals driven only by interannual wind stresses, or runoffs, or precipitation and a residual SSS signal driven by any other process. We therefore decompose SSS' in the REF experiment into contributions from interannual wind stress, interannual precipitation, interannual runoffs, and a residual as follows:

$$SSS'(REF) = SSS'(Tau_{int}) + SSS'(P_{int}) + SSS'(R_{int}) + SSS'(res) \tag{1}$$

The first three terms on the R.H.S. of (1) are obtained from the SSS' in the Tau<sub>int</sub>, P<sub>int</sub>, and R<sub>int</sub> experiments, respectively. They represent the contribution of wind stress SSS'(Tau<sub>int</sub>), oceanic precipitations SSS'(P<sub>int</sub>), and continental runoffs SSS'(R<sub>int</sub>) to the SSS'(REF). The first three terms on the R.H.S. of (1) do not add up exactly to the SSS'(REF) because of the influence of internal ocean variability related to eddies and of other nonlinearities. We obtain this last component as SSS'(res) = SSS'(REF) – SSS'(Tau<sub>int</sub>) – SSS'(P<sub>int</sub>) – SSS'(R<sub>int</sub>). A decomposition method similar to the one proposed in Vialard *et al.* [2013] is used to quantify the contribution of each of those components. The contribution of each component is computed by multiplying the correlation coefficients of each of the sensitivity experiment to the REF experiment by the standard deviation of the sensitivity experiment. The sum of contributions of each of the sensitivity experiments and residual gives the standard deviation of the REF experiment. This type of decomposition is used in Figures 7b–7e to assess these contributions to SSS'(REF) at the scale of the BoB and in Figures 9a, 10a, and 12a to assess these contributions to SSS'(REF) in the boxes of maximum variability.

We also assess the relationship between BoB SSS' and known interannual climate modes in the Indian Ocean, i.e., the IOD and ENSO. To characterize these modes, we have used standard indices. In the Pacific, ENSO is classically represented by the averaged SST anomalies over the Nino3.4 (120°W–170°W; 5°N–5°S) region during November–January. The Nino3.4 index is taken from [http://www.cpc.ncep.noaa.gov/products/analysis\\_monitoring/ensostuff/detrend.nino34.ascii.txt](http://www.cpc.ncep.noaa.gov/products/analysis_monitoring/ensostuff/detrend.nino34.ascii.txt). The IOD is represented by the dipole mode index (DMI) [Saji *et al.*, 1999] computed as the difference between interannual SST anomalies in the western (50°E–70°E; 10°N–10°S) and south-eastern equatorial Indian Ocean (90°E–110°E; 10°S–0°), averaged over the September–November season. The DMI index is taken from <http://www.jamstec.go.jp/frcgc/research/d1/iod/DATA/dmi.monthly.txt>. We will also use the interannual GB and PNR runoffs anomalies averaged over July–September. The indices above have been normalized by their standard deviation to obtain dimensionless indices. SSS' from REF and the sensitivity experiments are regressed on these indices to infer how these modes of variability control the SSS' evolution in different regions of the BoB (see Figures 9b, 10b, and 12b).

### 2.3. Mixed Layer Salinity Budget

One of the main goals of this work is to understand how oceanic and atmospheric processes act to regulate SSS IAV in the BoB. As a complement to the above sensitivity experiments, an analysis of the mixed layer salinity budget of REF simulation at interannual timescales is also performed. The mixed layer salinity budget used in the present study computes salinity tendency terms vertically averaged within the time-varying mixed layer depth and is similar to the one described in Akhil *et al.* [2014], who used this methodology to infer the processes responsible for SSS variations in the BoB at seasonal time scales. The model mixed layer depth is defined as the depth where density is 0.01 kg.m<sup>-3</sup> greater than surface density. Such a small criterion allows the vertically averaged salinity to be a good proxy for the SSS [de Boyer Montegut *et al.*, 2007]. In order to compute the ocean mixed layer salinity budget, the various terms contributing to salinity evolution are averaged over the mixed layer online, stored as 5 day averages, and grouped as follows:

$$\partial_t S = - \underbrace{\langle u \partial_x S + v \partial_y S \rangle}_a - \underbrace{\langle w \partial_z S \rangle}_b - \underbrace{\frac{1}{h} \frac{\partial h}{\partial t} (\langle S \rangle - S(z=h))}_c + \underbrace{\frac{(k \partial_z S)(z=h)}{h}}_d + \underbrace{\frac{(E-P-R)S}{h}}_e + \underbrace{\langle D_l(S) \rangle}_f \quad (2)$$

where brackets denote the vertical average over the time-varying mixed layer depth  $h$ ,  $S$  is the model salinity,  $(u, v, w)$  are the components of ocean currents,  $D_l(S)$  the lateral diffusion operator,  $k$  the vertical diffusion coefficient,  $E$  is the evaporation,  $P$  the precipitation, and  $R$  the river runoff. The term (a) represents the horizontal advection, (b) the vertical advection, (c) is the entrainment, (d) the vertical diffusion through the mixed layer base, (e) is freshwater flux forcing of the mixed layer, and (f) is lateral diffusion.

We use this salinity budget calculation to infer the respective contributions of these processes to the evolution of SSS IAV simulated by the REF experiment in the BoB. The term (f) for lateral diffusion is negligible and will not be considered in the following. The terms (b), (c), and (d) are grouped together in a vertical processes term. Our analyses will thus focus on identifying the relative influences of horizontal advection (a), vertical processes (b + c + d), and surface freshwater forcing (e). These three terms are regressed onto the normalized indices described in section 2.2 to infer the dominant processes affecting the SSS IAV in different regions of the BoB (see Figures 9c, 10c, and 12c).

#### 2.4. SSS Validation Data Sets

The realism of the REF simulation is assessed by comparing its SSS IAV to a comprehensive SSS dataset detailed in *Chaitanya et al.* [2014], which compiles all in situ SSS measurements available over the BoB during the 2006–2012 period. It consists of six different types of data: ARGO profilers [*Roemmich et al.*, 2009], ship-of-opportunity XCTD profiles and bucket measurements, RAMA moorings [*McPhaden et al.*, 2009], OMNI moorings [*Venkatesan et al.*, 2013], ship-of-opportunity thermosalinograph transects [*Alory et al.*, 2015] and dedicated hydrographic cruises. These six data sets are gridded by computing the median of all available individual measurements on a  $1^\circ \times 1^\circ \times 3$  months grid. Data gaps in the resulting gridded dataset are not filled, in order to avoid any spurious pattern in the merged product. We will also use the  $1^\circ \times 1^\circ$  monthly Aquarius SSS data set version 2.0 Level 3 provided by the NASA Jet Propulsion Laboratory (JPL) available from September 2011 to July 2015 (available from <ftp://podaac-ftp.jpl.nasa.gov/allData/aquarius/L3/mapped/CAPv3>) that has been shown to accurately capture the seasonal and SSS IAV in the BoB [*Akhil et al.*, 2016]. Interannual anomalies SSS' derived from these in situ and satellite SSS data are estimated by removing the North Indian Ocean Atlas (NIOA) SSS climatology [*Chatterjee et al.*, 2012].

### 3. Validation of Modeled Interannual SSS Variations

In this section, we first validate the modeled SSS IAV from REF to the in situ and remote sensing datasets described above.

Figure 2 displays the SSS' standard deviation from the gridded in situ data set (Figure 2a) and from the REF experiment (Figure 2b) over their common period (2006–2012). The regions of maximum SSS' variability agree qualitatively well between the two data sets. Both data sets indicate maximum amplitude of SSS IAV (above 0.6) along the northern and western basin, and minimum variability in the central BoB. Some discrepancies can however be noted, such as an underestimation of the modeled SSS IAV along the east coast of India and in the northern part of the domain between  $16^\circ\text{N}$  and  $18^\circ\text{N}$ . In addition, the model also displays a local maximum of SSS IAV in the Andaman Sea, where the lack of in situ observations prevents any validation.

A more detailed analysis of the model ability to capture the large-scale SSS' temporal evolution is provided in Figure 3 for regions of maximum variability outlined on Figure 2. The first subregion encompasses the northern part of the basin (NBoB,  $86^\circ\text{E}$ – $94^\circ\text{E}$ ;  $16^\circ\text{N}$ – $23^\circ\text{N}$ ) near the GB river mouth, where the largest SSS IAV is found in both the model and in situ observations. The second subregion is located in the western part of the BoB (WBoB,  $80^\circ\text{E}$ – $84^\circ\text{E}$ ;  $6^\circ\text{N}$ – $16^\circ\text{N}$ ) and encompasses the coastal region through which the seasonal NBoB freshening is transported southward during winter, as a narrow fresh tongue that hugs the eastern Indian coastline [*Akhil et al.*, 2014; *Chaitanya et al.*, 2014]. Model outputs also indicate a region of marked variability in the Andaman Sea (Figure 2b): this region is divided into two subdomains that exhibit distinct variations: the Northern Andaman sea (NANDA,  $94^\circ\text{E}$ – $99^\circ\text{E}$ ;  $12^\circ\text{N}$ – $18^\circ\text{N}$ ) and Southern Andaman sea (SANDA,  $94^\circ\text{E}$ – $99^\circ\text{E}$ ;  $6^\circ\text{N}$ – $12^\circ\text{N}$ ). The choice of the boundaries of these two subregions will be further justified in

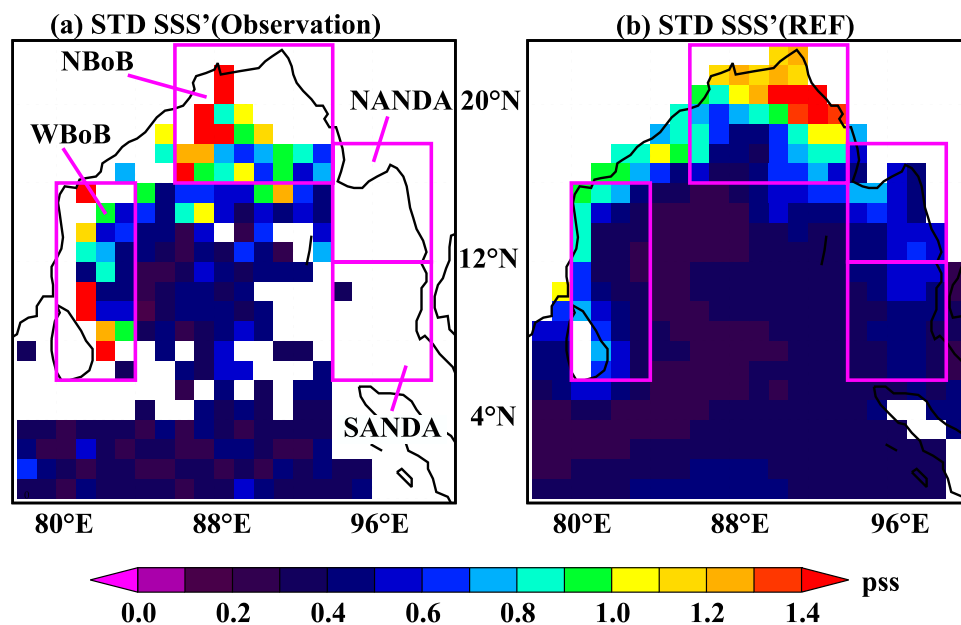


**Figure 2.** Standard deviation of BoB SSS' interannual anomalies SSS' for (left) observations and (right) model over their common period (2006–2012). The purple frames indicate four regions for future reference: the northern (NBoB, 86°E–94°E; 16°N–23°N) and western (WBoB, 80°E–84°E; 6°N–16°N) Bay of Bengal and the northern (NANDA, 94°E–99°E; 12°N–18°N) and southern (SANDA, 94°E–99°E; 6°N–12°N) Andaman Sea.

section 4. In the NBoB and WBoB regions, the model validation is performed by collocating model outputs with the in situ gridded product (thereby avoiding observations-free areas) over the common period (2006–2012) while the model cannot be validated over the Andaman Sea boxes (NANDA and SANDA) due to the lack of in situ observations there (Figure 2).

Modeled and observed SSS' evolution agree generally well over the NBoB with a correlation coefficient of 0.71 (Figure 3a). The observed SSS' evolution in this region exhibits successive periods of fresher-than-normal conditions and saltier-than-normal conditions, with anomalies ranging from  $-1$  pss to 1.5 pss. The model is able to accurately capture the timing and amplitude of the fresher-than-normal period from fall 2011 to spring 2012 (up to 0.7 pss of fresh anomaly), as well as the long-lasting salty period observed from summer 2009 to winter 2011. The shorter salty anomaly observed in fall 2007 is also captured by the model although it occurs 3 months later in the REF simulation (winter 2007). In the western box (WBoB, Figure 3b), the model is generally able to capture the timing of the strongest observed anomalous events (0.6 correlation), such as the anomalous freshening observed in fall 2010 and the anomalous salting observed in fall 2011. As already suggested by Figure 2, the model however underestimates the amplitude of SSS' IAV in the WBoB, for instance during the strong fall 2010 freshening. The model also exhibits strong anomalous events in the Andaman sea basin. In the northern Andaman box (NANDA, Figure 3c), the model exhibits a fresher-than-normal period centered around summer 2006 and saltier-than-normal period centered around summer 2007. In the southern Andaman box (SANDA, Figure 3d), an anomalous salting is simulated in fall 2010 while an anomalous freshening is evident in fall 2006.

Fall SSS' tends to be of opposite polarity in the WBoB and SANDA boxes regions ( $-0.73$  correlation, see Table 2). The variability in SANDA box is correlated moderately with that in NANDA box variability (0.49 correlation; see Table 2). Finally, the NBoB box does not show a coherent variability with any of the other regions discussed above.

Figure 3 suggests that fall is the season of largest SSS' IAV in the WBoB and SANDA box and one of the strongest in the NBoB box. The amplitude of SSS' IAV as a function of the season is further illustrated on Figure 4 for the model. The insufficient data coverage prevents us from providing an equivalent meaningful plot for observations. In NBoB, significant interannual variations (above 1.4 pss) appear during summer monsoon just offshore the mouth of the GB. These signals further strengthen and expand all over the box during fall, then weaken in winter and almost vanish during the subsequent year. In WBoB, interannual

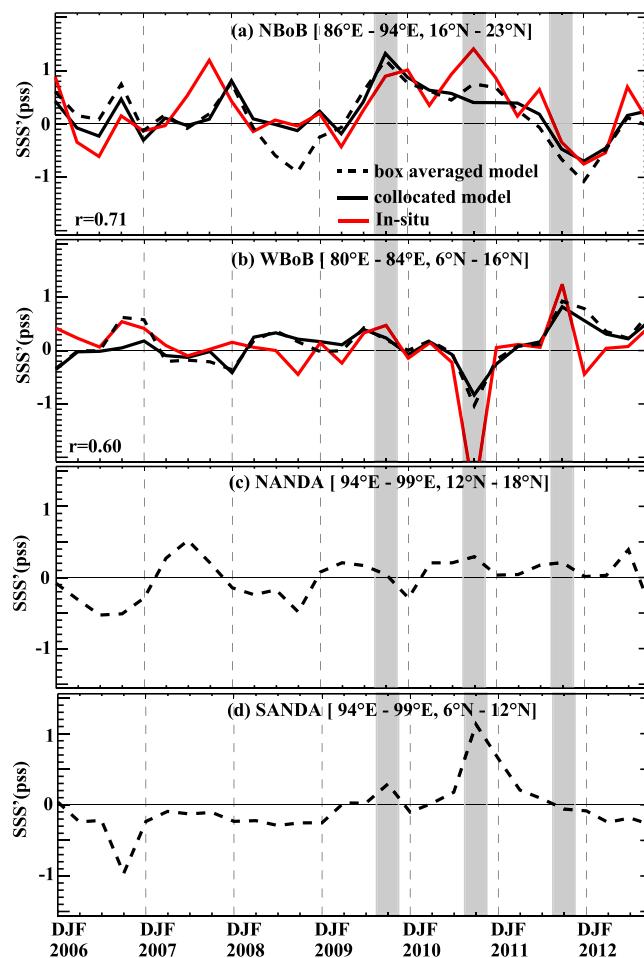


**Figure 3.** Time series of SSS interannual anomalies SSS' averaged over the (a) NBoB, (b) WBoB, (c) NANDA, and (d) SANDA boxes for observations (red), model subsampled at observation points (black), and full-box model average (dashed black). Observed time series are not available for the NANDA and SANDA boxes due to the scarcity of in situ data. DJF 2006 stands for December 2005 to February 2006, and so on. Shaded bands mark the SON 2009, 2010, and 2011 periods plotted on Figures 5 and 6.

display a strong salty pattern in the northern part of the Bay while the western part of the Bay exhibits an opposite signal, with fresh anomalies north and east of Sri Lanka (Figure 5b). The central part of the Bay displays fresh anomalies west of 88°E and salty anomalies east of it. Finally the southern part of the Bay exhibits salty anomalies south of 4°N. The model captures all these features accurately (Figure 5e). A large salty anomaly can also be noticed in the Andaman Sea (Figure 5e), a region that is not sampled by the in situ data set. Finally, fall 2011 is a period of general freshening in the northern part of the Bay (Figure 5c), although available in situ observations in the NBoB show more patchy patterns than during other periods

**Table 2.** Cross Correlation Between September–November Box-Averaged REF Experiment SSS Interannual Anomalies (See Figure 2 for Boxes Definition)<sup>a</sup>

	NBoB	WBoB	NANDA	SANDA
NBoB	<b>1</b>	-0.13	0.08	-0.06
WBoB		<b>1</b>	-0.1	<b>-0.73</b>
NANDA			<b>1</b>	<b>0.49</b>
SANDA				<b>1</b>

<sup>a</sup>Correlations that are significant at the 90% significance level are indicated in bold typeface (Student t-test with one degree of freedom per year).

signals are also largest in fall (above 1.4 pss) and still significant in winter (~0.8 pss) but are totally absent during spring and summer. Similar to WBoB box, the SANDA box displays largest SSS' in fall (> 0.9 pss) while they persist and shift westward in winter (~0.5 pss). Finally, interannual signals are prominent in the NANDA box during the summer monsoon near the Irrawaddy river mouth, whose interannual runoffs variations also display maximum variability at that season (Figure 1a; i.e., 0.96 mm/d).

From Figure 4, it is obvious that largest SSS' generally occur in fall, except for the NANDA region where largest variations occur in summer. Figure 5 therefore provides a detailed validation of the modeled SSS' spatial patterns to the in situ product for three successive fall seasons (i.e., fall 2009, 2010, and 2011) that are reasonably well sampled by the in situ data set. The availability of Aquarius data during fall 2011 allows additional validation of our model results. As already seen in Figure 3, fall 2009 exhibits large salty anomalies in the northern and western box along with weaker salty anomalies in the central part of the Bay (Figure 5a). Model data generally agree with this pattern, although the amplitude of the salty signal along the eastern coast of India is underestimated and along the central BoB is overestimated (Figure 5d). In fall 2010, observations display

a strong salty pattern in the northern part of the Bay while the western part of the Bay exhibits an opposite signal, with fresh anomalies north and east of Sri Lanka (Figure 5b). The central part of the Bay displays fresh anomalies west of 88°E and salty anomalies east of it. Finally the southern part of the Bay exhibits salty anomalies south of 4°N. The model captures all these features accurately (Figure 5e). A large salty anomaly can also be noticed in the Andaman Sea (Figure 5e), a region that is not sampled by the in situ data set. Finally, fall 2011 is a period of general freshening in the northern part of the Bay (Figure 5c), although available in situ observations in the NBoB show more patchy patterns than during other periods (Figures 5a and 5b) with both positive and negative pixels. A large salty anomaly is also observed on the western side of the BoB. SSS' in the central part of the Bay are quite patchy. The model reproduces very well the salty anomaly in the WBoB (Figure 5f) but does not accurately capture the more complex SSS' structure seen in the central and northern part of the Bay,

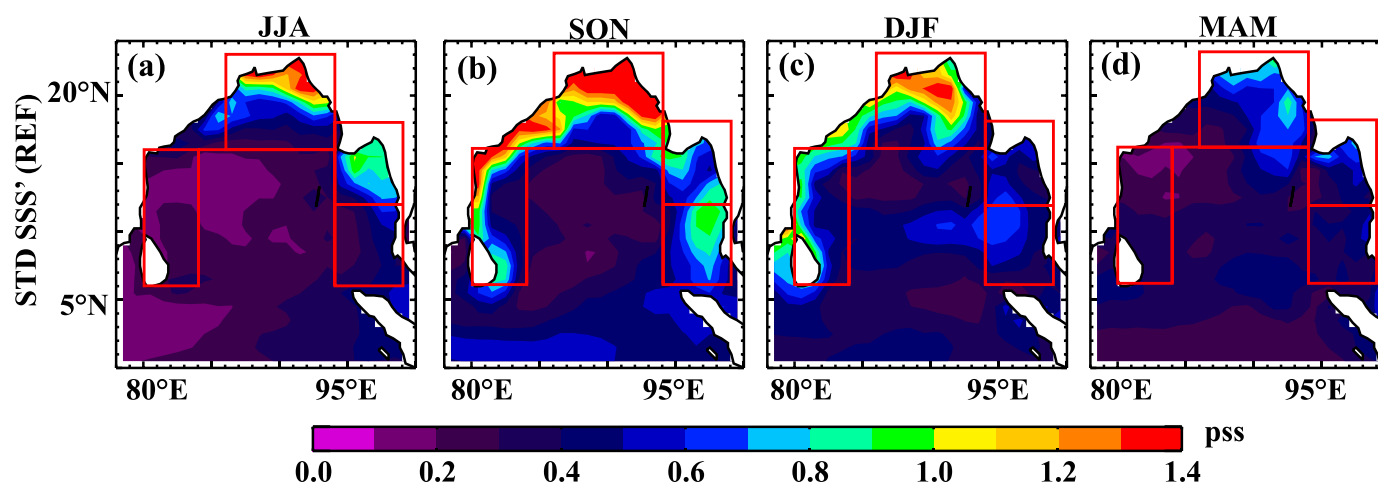


**Figure 4.** Standard deviation of reference experiment interannual SSS anomalies  $SSS'(REF)$  for (a) June–August (JJA), (b) September–November (SON), (c) December–February (DJF), and (d) March–May (MAM).

although box-averaged  $SSS'$  in NBoB is fresher than normal for both model and observations (Figure 3a). The availability of Aquarius from 2011 allows us to compare the model  $SSS'$  pattern everywhere in the Bay with this satellite product (Figure 5g). These two data sets agree quite well. There are however two obvious flaws: first, the salty signal along the east coast of India expands as far north as  $20^\circ N$  in the model while it is restricted to the south of  $16^\circ N$  in the satellite data. Second, the model exhibits a salty signal throughout the Andaman Sea, although Aquarius indicates a fresh signal over the northeastern half of it. While the first flaw is most probably related to a model deficiency, the second one is harder to interpret, in the absence of in situ ground truth over the Andaman Sea.

The above diagnostics therefore demonstrate that the model generally captures the main patterns of BoB  $SSS$  IAV: maximum variability for both model and observations are indeed found in the same regions and modeled and observed year-to-year  $SSS$  variations over the regions of maximum variability are in good agreement, in both timing and magnitude. The data coverage is too sparse to allow a detailed description of  $SSS$  IAV from observations everywhere in the Bay. The good agreement between model and observed interannual variability however gives us confidence in analysing the model outputs to decipher the mechanisms of  $SSS$  IAV in the BoB in more details.

#### 4. Patterns and Mechanisms of BoB Interannual SSS Variability

In section 4.1, we first provide a basin-scale estimate of the relative importance of each forcing term (wind stress, precipitation, and runoff) in driving  $SSS$  IAV. Section 4.2 then describes the main patterns of  $SSS$  IAV using an empirical orthogonal function (EOF) analysis and relates this variability to known climate modes. Section 4.3 details how IOD events control to a large extent the  $SSS$  IAV in the WBoB and SANDA regions through the analysis of the sensitivity experiments and mixed layer salinity budget described in section 2. Section 4.4 addresses the influence of the GB fluctuations on  $SSS$  IAV in NBoB region using similar diagnostics. The  $SSS$  IAV in the NANDA box is finally briefly discussed in the last subsection.

##### 4.1. Respective Contributions of Wind and Freshwater Fluxes

Figure 6 provides a first illustration of  $SSS'$  simulated by each sensitivity experiment for the 2009–2011 consecutive fall seasons depicted in Figure 5. For those 3 years,  $SSS'$  are generally quite similar in the reference simulation and in the  $Tau_{int}$  sensitivity experiment (Figures 6a–6f). This suggests that interannual wind stress variations play an important role in controlling  $SSS$  IAV everywhere in the Bay for the 2009–2011 period.  $SSS'$  driven by rainfall interannual anomalies are very modest (Figures 6g–6i), suggesting that interannual precipitations do not play a strong role in shaping  $SSS$  IAV, except in the coastal regions in the northeastern part of the Bay where moderate and coherent positive and negative signals are obvious in 2010 and 2011. Results from  $R_{int}$  are more contrasted (Figures 6j–6l), with a weak response to runoff interannual anomalies in fall 2010 and 2011, but a larger signal along the eastern coast of India north of  $15^\circ N$  in

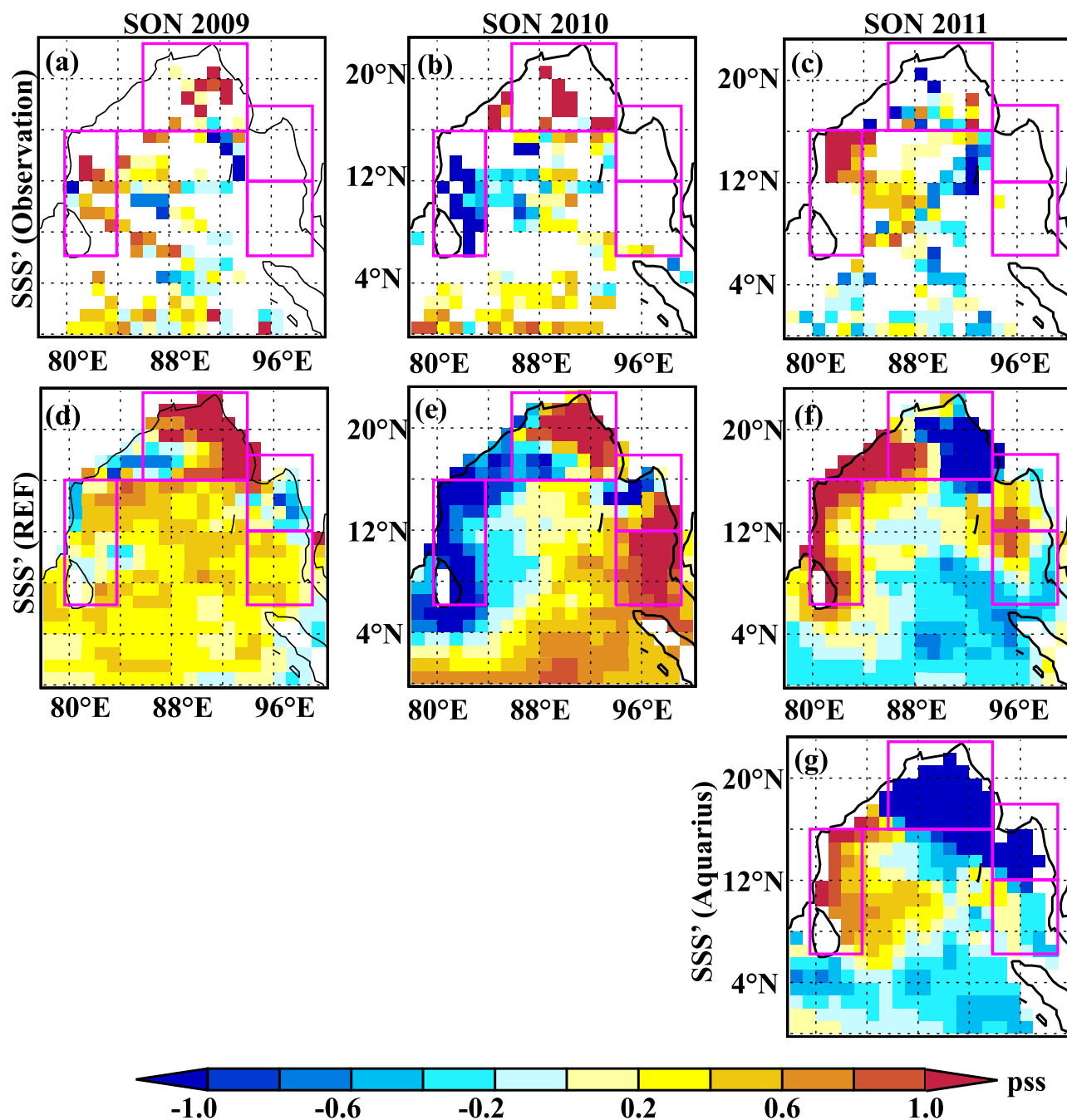


**Figure 5.** SSS interannual anomalies  $SSS'$  from (first row) in situ observations, (second row) REF simulation, and (third row) satellite observations for (first column) SON 2009, (second column) SON 2010, and (third column) SON 2011. Aquarius satellite data are only available from 2011 onward.

fall 2009. For this year and location,  $R_{int}$  favors a salty signal that opposes the fresh signal promoted by  $\tau_{int}$ , resulting in rather weak  $SSS'$  in the reference simulation. In the northeastern BoB on the other hand,  $R_{int}$  and  $\tau_{int}$  both induce positive  $SSS'$  (with comparable contribution of each of the two).

A quantitative estimate of the contributions from wind-driven circulation, rainfall, river runoffs, and nonlinearities to the total SSS IAV (Figure 7a) is obtained from the  $\tau_{int}$ ,  $P_{int}$ , and  $R_{int}$  sensitivity experiments, as explained in section 2.2 (Figures 7b–7e). These contributions are calculated at each grid point as the correlation of  $SSS'$  in each sensitivity experiment (and the residual to  $SSS'$  in REF) to REF  $SSS'$ , multiplied by their standard deviation (see section 2.2 for details). With such a normalization Figures 7b–7e add up to the  $SSS'$

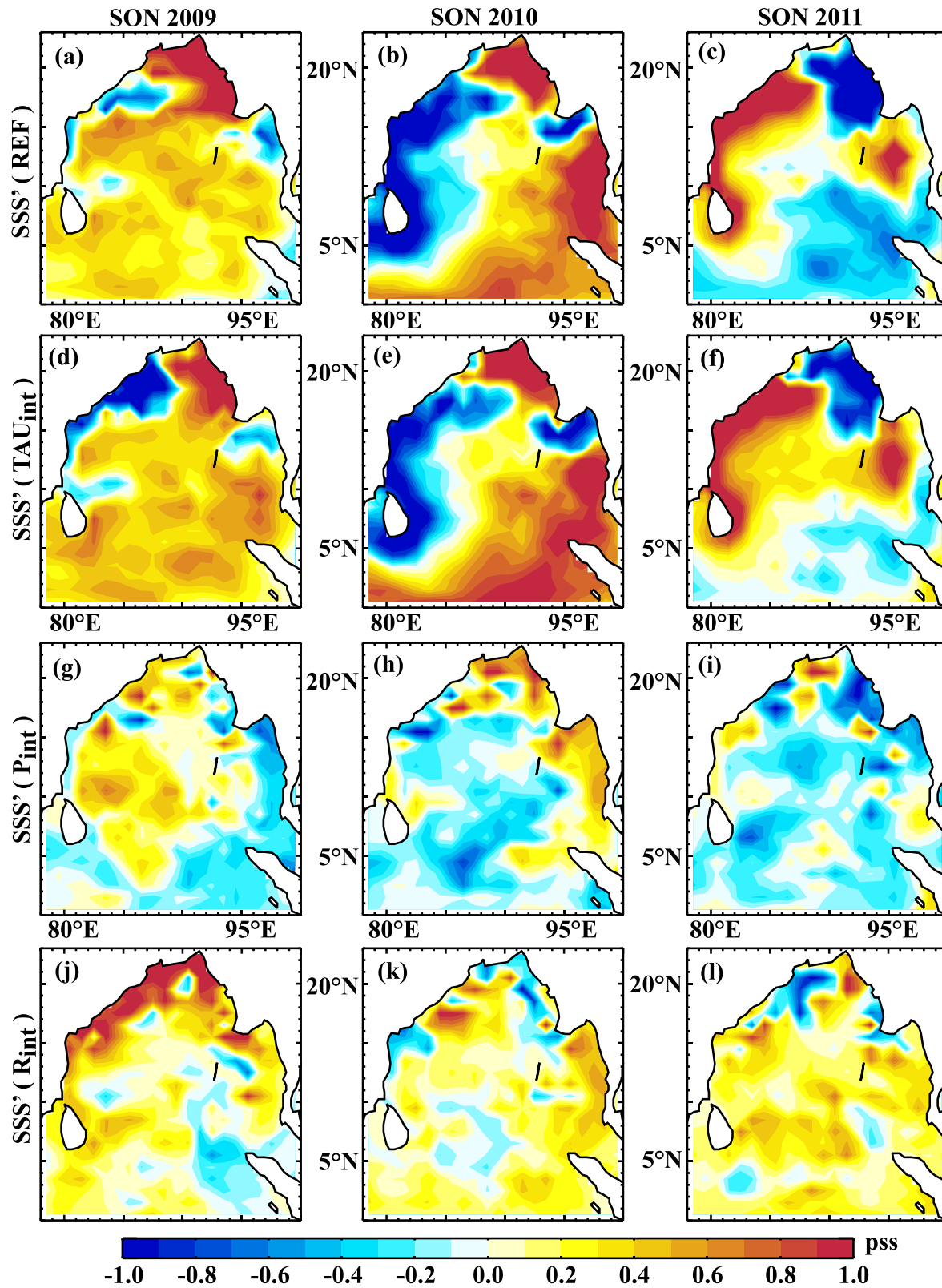


**Figure 6.** SSS interannual anomalies SSS' from (first row) REF, (second row) TAU<sub>int</sub>, (third row) P<sub>int</sub>, and (fourth row) R<sub>int</sub> experiments (see Table 1) in (first column) SON 2009, (second column) SON 2010, and (third column) SON 2011.

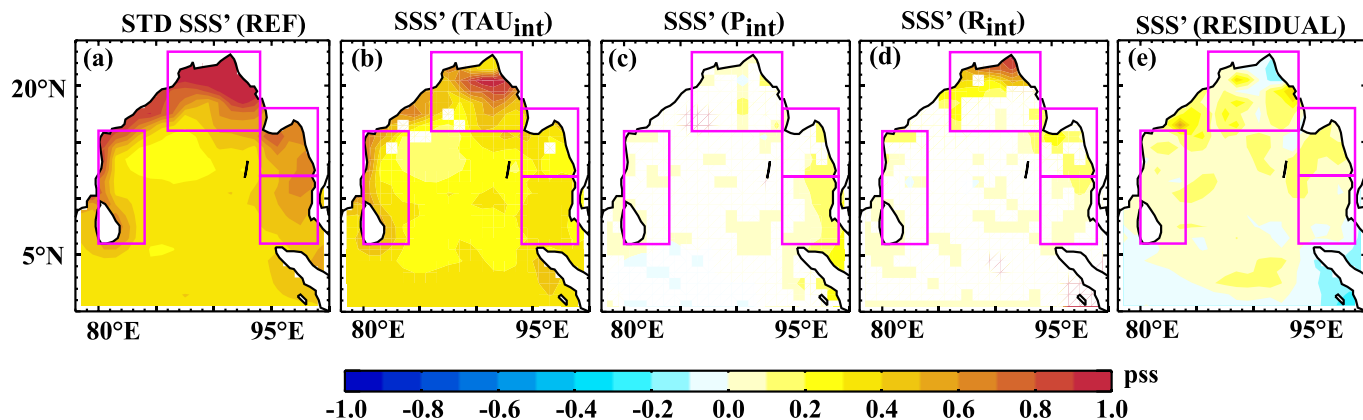


**Figure 7.** (a) Maps of REF experiment SSS interannual anomalies SSS'(REF) standard deviation and contribution of interannual anomalies of various forcings to the SSS'(REF) standard deviation: (b)  $\text{TAU}_{\text{int}}$ , (c)  $\text{P}_{\text{int}}$ , (d)  $\text{R}_{\text{int}}$ , and (e) Residual ( $\text{REF} - (\text{TAU}_{\text{int}} + \text{P}_{\text{int}} + \text{R}_{\text{int}})$ ). These contributions are computed as the correlation of SSS' in each of the sensitivity experiments and residual to the SSS'(REF), multiplied by their standard deviation (by construction, Figures 7b–7e add up to Figure 7a). The regions where the contribution by the residual terms is larger than the contribution of Figures 7b–7d are masked.

standard deviation in REF, shown on Figure 7a. Wind-driven circulation anomalies are the main contributor to the total SSS IAV, in particular south of the GB river mouth and along the east coast of India (Figure 7b). River runoffs only contribute to the SSS IAV locally near the GB river mouth, and not very much over the rest of the basin (Figure 7d). Interannual precipitations variability does contribute much to the SSS IAV anywhere, except in the southern Andaman Sea (Figure 7c). Figure 7e shows the contribution of the residual, which accounts for nonlinearities among the different forcing including internal instabilities (i.e., mesoscale eddies) as well as nonlinear combination of physical processes (e.g., the wind effect on the mixed layer depth will modulate the dilution of atmospheric or continental freshwater fluxes). Although this nonlinear contribution has a relatively large amplitude south of the GB river mouth (not shown), it is poorly correlated to SSS' in REF, i.e., it does not explain much of the total SSS IAV. This is probably partly due to the fact that this residual term in particular represents the signature of mesoscale eddies, that generally have a random phase with respect to lower-frequency, larger-scale SSS fluctuations associated with climate variability.

#### 4.2. Main Patterns of SSS' Variability

BoB SSS IAV being larger in fall (see Figure 4), the main patterns of SSS interannual variability are extracted by applying an EOF analysis in the BoB ( $78^{\circ}\text{E}–100^{\circ}\text{E}$ ;  $0^{\circ}\text{N}–23^{\circ}\text{N}$ ) during this season. The first two modes, respectively, explain 37% and 24% of the SON SSS IAV, while the third mode only explains 10%. We will therefore focus on the first two EOF modes in the following. The first two EOF modes in fall and their corresponding principal components are displayed on Figure 8.

The first EOF pattern is characterized by a saltening signal along the eastern coast of India and Sri Lanka (WBoB box) and a freshening signal south of the GB river mouth and in the southern part of the BoB (south of  $\sim 5^{\circ}\text{N}$ ) and southern Andaman Sea (SANDA box). This opposite variability in the WBoB and SANDA regions derived from this EOF analysis is consistent with the negative correlation between SSS' averaged over the two regions in that season ( $-0.73$ ; see Table 2). This pattern is reminiscent of the simulated SSS' pattern in fall 2011, characterized by strong salty anomalies along the eastern coast of India and fresh anomalies in the northeastern BoB, southern BoB, and southern Andaman Sea basin (Figure 6c). The EOF1 pattern is also opposite to the SSS' pattern simulated in fall 2010 (Figure 6b). These 2 years were characterized by a negative IOD event in fall 2010 and a positive IOD event in fall 2011 [McPhaden and Nagura, 2014]. To further ascertain the relationship between the first mode of SSS IAV and IOD variability, Figure 8a displays the evolution of the first EOF principal component (PC1) along with the DMI index. The two time series closely match, with a 0.88 correlation, indicating that IOD events are responsible for most of the SSS' variations depicted by EOF1. The PC1 also displays a weaker but significant correlation with ENSO (0.63), presumably because of the tendency of ENSO and IOD events to cooccur. On the other hand, it exhibits a weak correlation with GB runoffs ( $-0.43$ ). This PC is also poorly correlated with PNR runoffs (0.24) along the

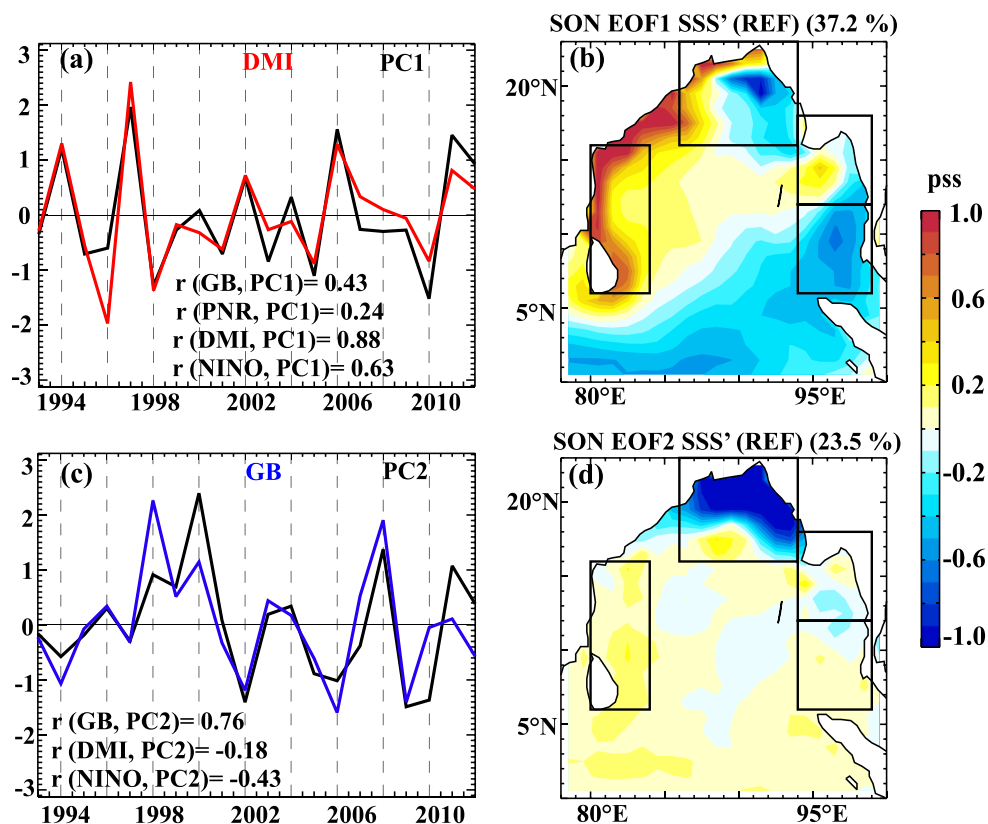


**Figure 8.** Principal component of the (a) first (PC1) and (c) second (PC2) empirical orthogonal function (EOF) analysis of September–November reference experiment interannual SSS anomalies SSS'(REF) and their correlation with the July–September Ganga-Brahmaputra (GB) and east coast of India rivers (PNR) runoff, September–November Dipole Mode Index (DMI), November–January ENSO index (NINO). (b,d) Corresponding EOF patterns.

eastern coast of India, suggesting that local continental freshwater fluxes only marginally influence the SSS IAV along the east coast of India.

The second EOF is characterized by a strong freshening confined to the northern part of the BoB (NBoB region), with very weak SSS' anywhere else in the Bay (Figure 8d). An obvious candidate for driving this pattern of variability is the local influence of the interannual fluctuations of the neighboring GB river discharge. The second EOF principal component (PC2) and the July–September-averaged GB river runoff time series are indeed strongly related to each other, with a 0.76 correlation (Figure 8c). On the other hand, the correlation between PC2 and PNR is rather poor ( $-0.26$ ). PC2 is not correlated with the IOD index ( $-0.18$ ), but weakly correlated with ENSO ( $-0.43$ ) presumably because of the influence of ENSO on summer monsoon rainfall over the Ganges-Mahanadi watershed [e.g., Vecchi and Harrison, 2004].

The simple analysis provided on Figure 8 suggests that SSS IAV in the BoB in fall can be described by two modes of variability. The first mode is characterized by opposite SSS' along the eastern coast of India (WBoB box) and in the Southern Andaman Sea (SANDA box) and is strongly tied to the IOD variability. The second mode is characterized by SSS IAV confined to the northern Bay (NBoB box) and is locally driven by interannual anomalies of the GB river runoff. Table 3 shows the correlation of fall SSS' in each of the boxes of maximum variability with the time variations of PC1, PC2, DMI index, and GB interannual runoffs fluctuations averaged over JAS. This table shows that fall SSS IAV in the WBoB and SANDA regions is largely captured by EOF1 (0.96 and  $-0.72$  correlation with PC1 respectively) and strongly related with IOD variations (0.81 and  $-0.73$  correlation with DMI respectively). In section 4.3, we will hence detail the processes responsible for the SSS IAV in WBoB and SANDA regions and how the IOD influence operates in this region by evaluating the respective contributions of freshwater fluxes and dynamical processes to SSS IAV in REF experiment through the analysis of the sensitivity experiments and mixed layer salinity budget described in section 2.

**Table 3.** Correlation of September–November Average SSS Interannual Anomalies in the Reference Experiment—SSS'(REF)—in Each Box With: The Principal Components PC1 and PC2 of the First and Second Mode of the Empirical Orthogonal Function (EOF) Analysis of the BoB SSS'(REF); The September–November Average IOD Index (DMI for Dipole Mode Index); the July–September Ganga–Brahmaputra Runoff (GB)<sup>a</sup>

	NBoB	WBoB	SANDA
PC1	−0.14	<b>0.96</b>	−0.72
PC2	−0.97	−0.02	0.17
DMI	0.18	<b>0.81</b>	−0.73
GB	−0.76	−0.31	<b>0.46</b>

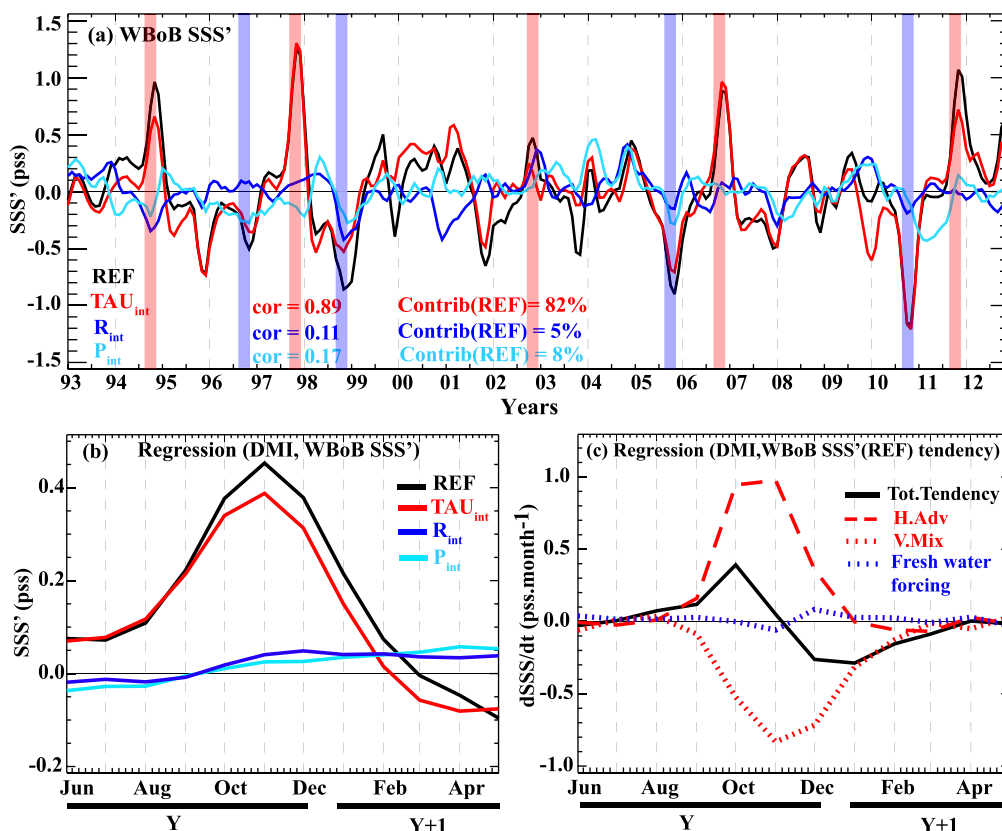
<sup>a</sup>Correlations that are significant at the 90% significance level are indicated in bold typeface (Student t-test with one degree of freedom per year).

Table 3 also illustrates that NBoB SSS IAV is largely depicted by EOF2 (−0.97 correlation with PC2) and strongly related to interannual GB variations (−0.76 correlation with GB interannual runoffs fluctuations averaged over JAS). We will hence similarly investigate the processes responsible for the SSS IAV in the NBoB region and how the influence of GB runoffs fluctuations operates in section 4.4. The fourth region of maximum variability, i.e., the NANDA

region, is neither strongly related to any PC nor to IOD or GB interannual fluctuations: the diversity of the processes influencing the NANDA region will be qualitatively discussed in section 4.5.

### 4.3. SSS Response to IOD Events

Figures 9 and 10 provide a detailed description of the processes driving SSS' in the WBoB and SANDA regions and their relationship with IOD variability. Figures 9a and 10a first provide SSS' time series from the reference and each sensitivity experiment averaged over the WBoB and SANDA boxes, respectively. As



**Figure 9.** (a) Time series of monthly average WBoB SSS interannual anomalies in REF (black),  $\tau_{int}$  (red),  $P_{int}$  (light blue), and  $R_{int}$  (deep blue) experiments. The correlation and relative contributions of the interannual variability of each forcing to SSS'(REF) are indicated on Figure 9a, along with positive (red-shading) and negative (blue-shading) IOD events. Regression to the September–November normalized DMI index of (b) monthly WBoB SSS' in REF (black),  $\tau_{int}$  (red),  $P_{int}$  (light blue), and  $R_{int}$  (deep blue) experiments and of (c) monthly SSS tendency terms interannual anomalies from REF, including total tendency (time derivative of mixed layer salinity, black curve), horizontal advection (sum of zonal and meridional advection, red-dashed curve), vertical mixing (sum of vertical advection, entrainment, and vertical diffusion through the mixed layer base, red dotted curve) and freshwater forcing (sum of evaporation, precipitation, and runoff, blue-dotted curve).

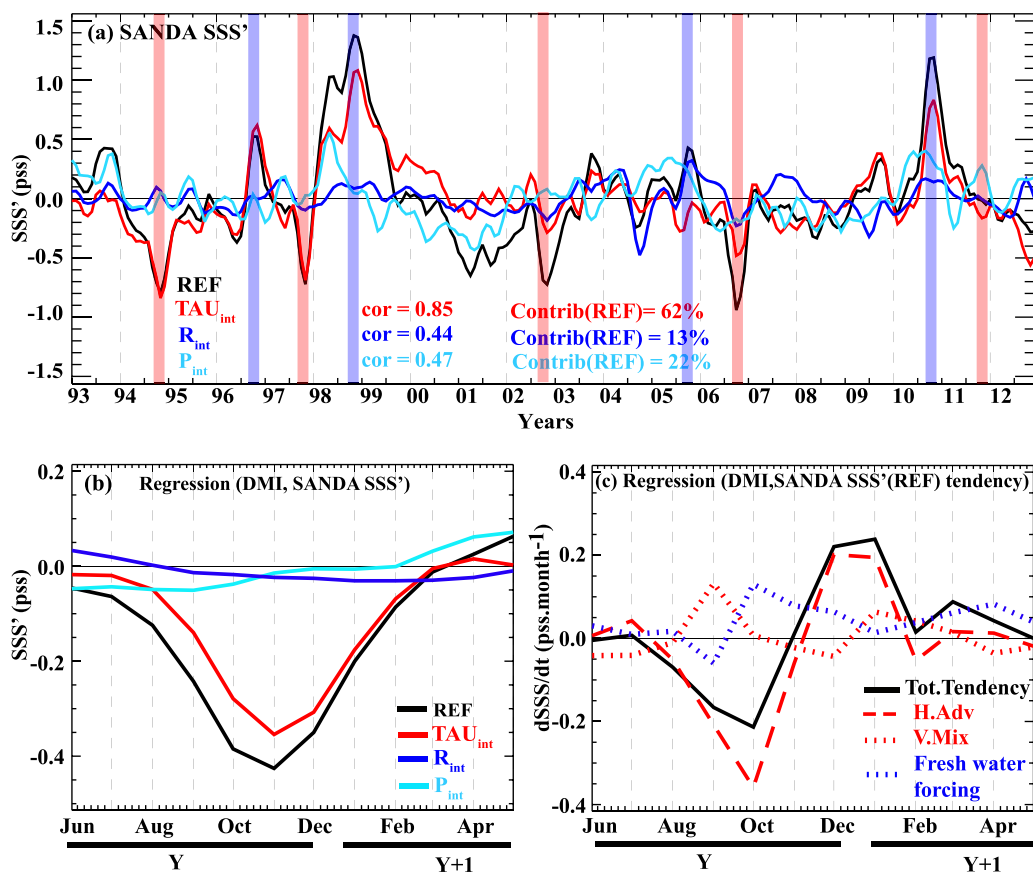
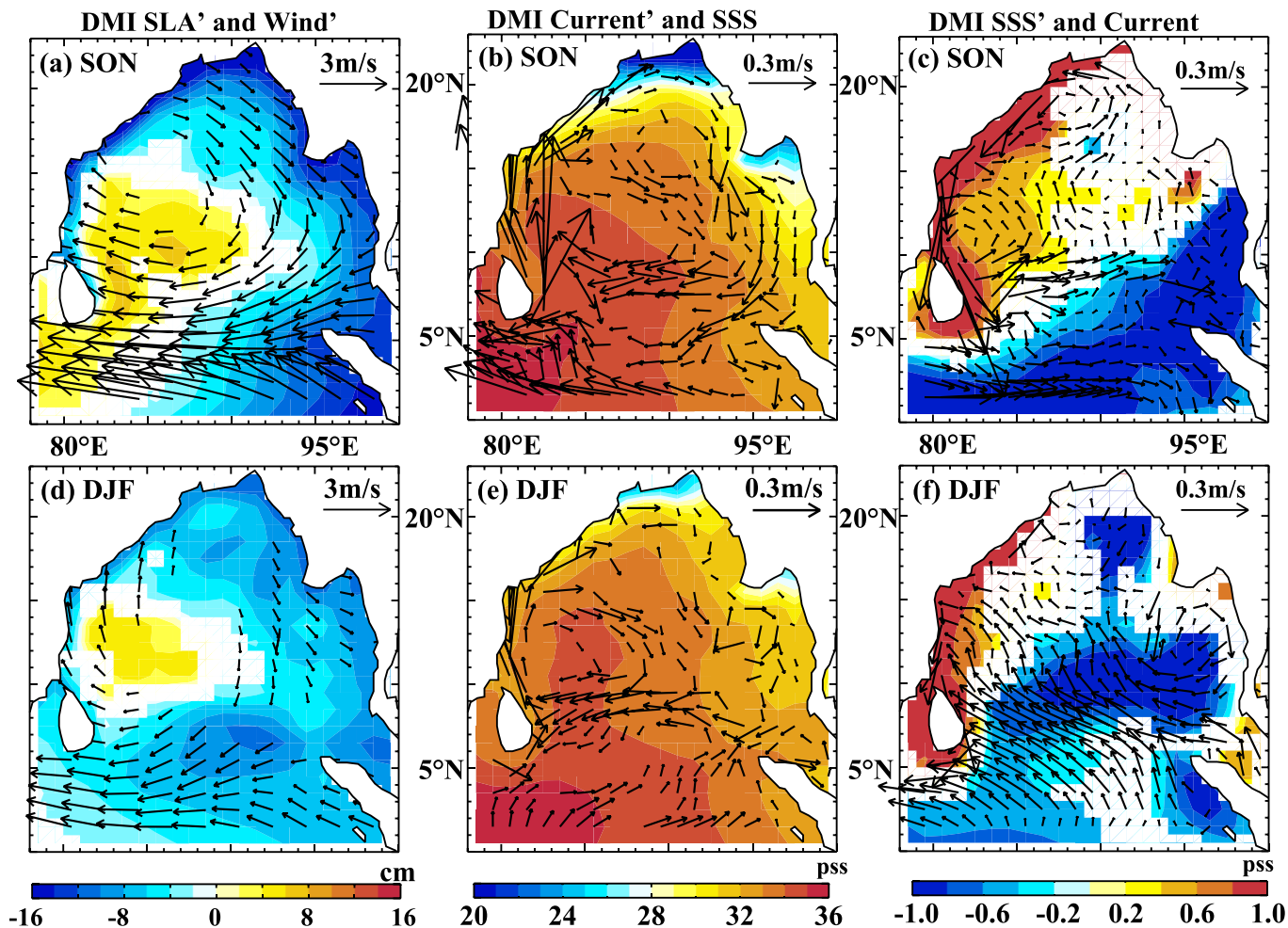


Figure 10. As Figure 9, but for SANDA box.

expected, these panels show that positive IOD events (red shading in fall 1994, 1997, 2002, 2006, and 2011) are generally associated with salty anomalies in WBoB and fresh anomalies in SANDA in REF simulation (black curves). Similarly, negative IOD events (blue frames in fall 1996, 1998, 2005, and 2010) are associated with fresh anomalies in WBoB and salty anomalies in SANDA in REF simulation.  $SSS'(Tau_{int})$  (red curves) display a very similar evolution to  $SSS'(REF)$  in both WBoB and SANDA regions, while  $P_{int}$  and  $R_{int}$  experiments yield considerably weaker  $SSS'$  (dark blue and light blue curves), pointing the dominant role of interannual wind stress in driving  $SSS'$  in these two regions. Interannual wind stress fluctuations indeed explain 82% of  $SSS'(REF)$  in WBoB over the entire period (0.89 correlation between  $SSS'(Tau_{int})$  and  $SSS'(REF)$ ) and 62% in SANDA box (0.85 correlation), with precipitation and runoff having a considerably weaker impact in these two regions.

The typical  $SSS'$  evolution during a positive IOD events is further illustrated on Figures 9b and 10b for the WBoB and SANDA regions, respectively: a positive IOD event is associated with a gradual  $SSS'(REF)$  increase (resp. decrease) in WBoB (resp. SANDA) from August, reaching its peak in November ( $\sim 0.45$  pss) and decaying from December–February (black curves on Figures 9b and 10b). As already suggested by Figures 9a and 10a, most of this IOD-related  $SSS'$  IAV in WBoB and SANDA is dynamically driven (red curve on Figures 9b and 10b), IOD-related freshwater fluxes playing a minor role (dark blue and light blue curves on Figures 9b and 10b).

The wind stress can contribute to the  $SSS'$  IAV in two ways: through horizontal advection (term  $a$  of equation (1)) and through vertical processes that gather the influence of vertical advection (term  $b$  of equation (1)), entrainment (term  $c$  of equation (1)), and the vertical diffusion through the mixed layer base (term  $d$  of equation (1)). Figures 9c and 10c allow to reveal how the wind stress influences the  $SSS'$  tendency terms during a positive IOD event. For both regions, the growth of the  $SSS'$  is driven by the anomalous horizontal advection term (dashed red curves) from August to October during positive IOD events.



**Figure 11.** (a) Regression of Sea level (SL) (color) and wind (vectors), (b) and surface currents (vectors) interannual anomalies onto the September–November Dipole Mode Index (DMI). The September–November average climatological SSS (color) are plotted on Figure 11b and (c) climatological currents (vectors). (d–f) Same for DJF. The regression coefficients for wind, current, sea level, and SSS anomalies are only plotted when significant at the 90% confidence level.

Figure 11 illustrates how the IOD variability drives anomalous horizontal SSS advection in these two regions. A positive IOD drives negative sea level anomalies all along the rim of the BoB in fall (Figure 11a). This sea level signal is consistent with an upwelling coastal Kelvin wave propagating into the BoB coastal waveguide. This IOD-related upwelling coastal Kelvin wave originates from the equatorial waveguide, where it is forced by equatorial easterlies in fall [Aparna *et al.* 2012], but is probably also reinforced by southward alongshore wind stresses in the eastern BoB (Figure 11a). The resulting negative sea level anomalies drive an anticyclonic circulation around the rim of the Bay in fall (Figure 11b), with southward currents anomalies in the Andaman Sea and northward currents anomalies along the east coast of India. Northward currents anomalies along the east coast of India indeed reflect a weakening of the climatologically southward flowing EICC after the monsoon (vectors in Figure 11c), that will act to reduce the southward advection of fresh waters from the northern Bay in that season and to translate into salty anomalies in WBoB (color in Figure 11c) [Akhil *et al.*, 2014; Chaitanya *et al.*, 2014]. Similarly, the southward currents anomalies in the Andaman Sea region (vectors in Figure 11b) will foster anomalous advection of freshwaters from the northern to the southern Andaman Sea and hence drive the anomalous freshening seen in the SANDA region in fall (color in Figure 11c). The role of anomalous horizontal advection by IOD-related alongshore current anomalies in driving these salty SSS' is further confirmed by the strong correlation existing between the meridional currents anomalies and SSS' in fall in the WBoB (0.92) and SANDA regions (0.63).

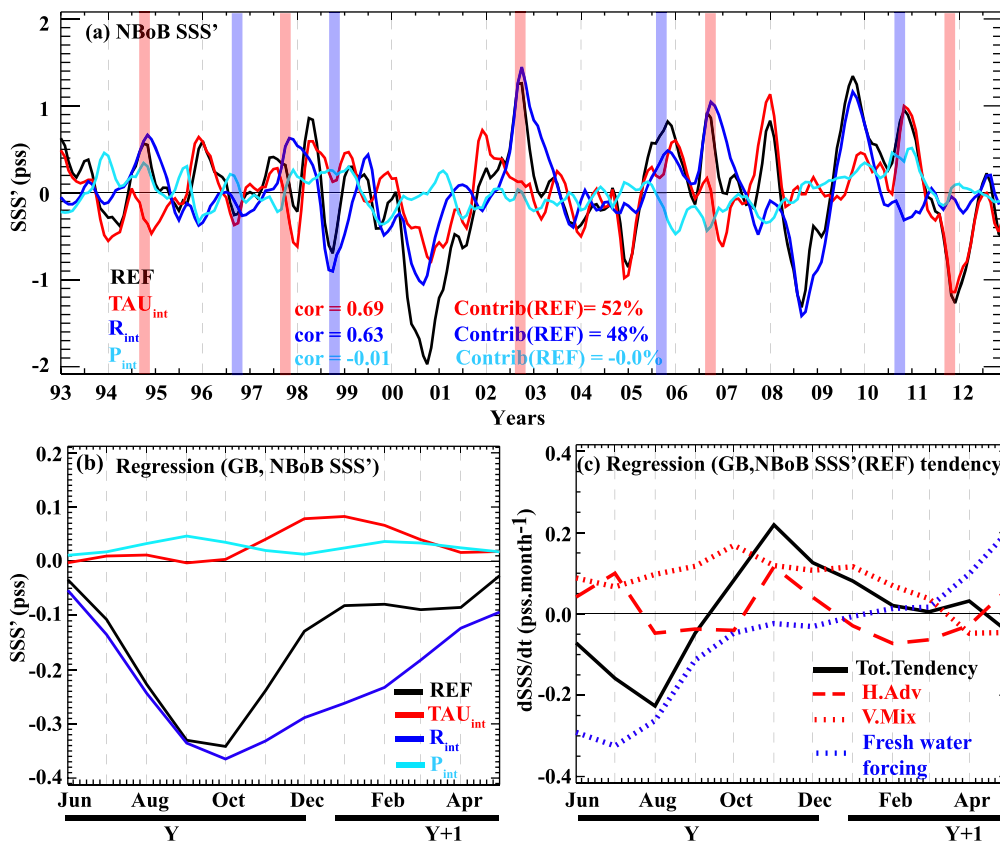


Figure 12. As Figure 9, but for NBoB box.

While Figures 9c and 10c clearly indicate that anomalous horizontal advection drives the growth of SSS' from August to October in both WBoB and NANDA regions during IOD events, the processes driving the decay of the SSS' in these two regions from November onward are different. In WBoB, Figure 9c shows that vertical processes are responsible for this decay: they generally damp the saltening tendency by anomalous horizontal advection during from August to October to finally overcome it from November onward, hence driving SSS' decay in winter. This anomalous freshening tendency through vertical processes can be interpreted as follows: saltier than usual SSS in WBoB results in a reduced vertical salinity gradient in the upper ocean, resulting in a weaker upward salt flux from vertical processes. The freshening tendency through vertical processes finally overcomes the saltening tendency from November onward, acting to erode the SSS' generated by the IOD-related horizontal currents in the WBoB (Figure 9c). In the SANDA, Figure 10c reveals that, as for the growth phase, horizontal advection is also responsible for the decay of the fresh anomalies from November onwards. Climatological north-westward currents in the southern part of the BoB near 10°N in winter (vector in Figure 11f) indeed act to advect the fresh SSS' from the Andaman Sea to the central part of the Bay (color in Figure 11f), resulting in a decay in the freshening in the SANDA region.

#### 4.4. SSS IAV Generated by GB Runoffs Fluctuations

While the WBoB and SANDA SSS IAV is strongly driven by IOD variations, NBoB interannual SSS' fluctuations are largely controlled by GB runoffs during fall (see Table 3 and section 4.2). Figure 12 provides a detailed description of the processes driving the NBoB SSS IAV and its relationship with both GB runoffs and IOD variability. Figure 12a first provides average NBoB SSS' time series from REF and each sensitivity experiment. This figure illustrates that the relative influence of each process strongly depends on the period. Precipitation does not generally play a significant role, except during some peculiar periods (e.g., 1998, 2006, and 2010). Strong interannual anomalies are mainly explained by runoffs variations in some epochs (e.g., 2008 freshening) while wind variations play a dominant role during other epochs (2010–2012). In other instances,

the influence of wind and runoff forcing add up (e.g., 2000) or oppose each other (e.g., 2007). This results in a similar correlation of  $SSS'(Tau_{int})$  and  $SSS'(R_{int})$  to  $SSS'(REF)$  in the NBoB box (Figure 12a; 0.69 and 0.63 correlation, respectively), with  $SSS'(Tau_{int})$  and  $SSS'(R_{int})$  explaining, respectively, 52% and 48% of  $SSS'(REF)$ . In contrast to WBoB and SANDA regions where wind stress variability dominates SSS IAV in all seasons, the respective contribution of wind stress and runoffs to SSS IAV in NBoB is however strongly variable from one season to another (not shown): runoffs interannual variations dominate NBoB SSS IAV in summer (60% contribution) and fall (80% contribution), while NBoB SSS IAV is dominated by wind stress interannual variations in winter (85% contribution) and spring (70% contribution).

The typical influence of GB interannual fluctuations onto NBoB SSS' evolution is further illustrated in each experiment on Figure 12b: increased GB runoff at the end of the summer monsoon induces anomalously fresh SSS in NBoB from June to October with a sharp decline from November to December (black curve on Figure 12b). As expected, this SSS' evolution is largely driven by runoffs variations (blue curve on Figure 12b), with a significant contribution of wind stress variations during the decay phase (red curve on Figure 12b). Figure 12c allows to further discuss how the influence of GB runoff fluctuations operate by providing the typical evolution of the SSS' tendency terms for larger than usual GB runoffs. This analysis confirms that freshwater forcing (dashed blue curve) largely drives the freshening phase from June to October (plain black curve) but cannot explain the decay phase. This decay is largely controlled by the anomalous saltening driven by vertical processes from June to next February (dashed red curve on Figure 12c). Larger than usual GB runoffs result in fresher surface waters and a shallower and sharper halocline from summer to the next winter. These halocline variations act to strengthen the upward salt flux, inducing an anomalous saltening from vertical processes that eventually overcomes the surface freshening through increased runoffs and drive the surface freshening decay from October onward.

While these mechanisms related to GB runoff fluctuations largely explain NBoB SSS IAV in summer and fall, wind stress fluctuations dominate NBoB SSS IAV in winter and spring. This is most likely because, while river runoffs dominate SSS' in the immediate vicinity of the GB river mouth (Figure 7d), interannual wind stress variations contribute more strongly in the southern half of the NBoB box (Figure 7b). Once the GB interannual variations have setup a SSS interannual anomaly, wind stress interannual fluctuations indeed play a strong role in how they evolve and spread over the entire NBoB box, through their effects on both locally wind-driven current anomalies and vertical mixing.

#### 4.5. The Northern Andaman Sea Region

SSS IAV in the NANDA box is largely independent from the IOD variability (Correlation between SON DMI and NANDA SSS' of  $-0.02$ ) and only moderately correlated with the SANDA box (0.49, Table 2). The SSS IAV in this region is governed by a more complex combination of processes than for other regions and is briefly discussed from Figure 13. In this region, wind stress, precipitations, and runoffs interannual variations all contribute to SSS IAV, respectively, explaining 30%, 28%, and 28% of SSS' variability (Figure 13a). The dominant process driving SSS IAV varies strongly from year to year, with for example a dominant effect of wind stress in early 1998, dominant effect of runoff in late 2005, and dominant effect of rain in 2010. The dominant process also varies strongly from season to season (not shown). It is in summer that NANDA SSS IAV is most clearly related to a single process: runoffs fluctuations from the Irrawaddy (Figure 13b). Summer (June–August) SSS' exhibits a  $-0.74$  correlation with JJA Irrawaddy runoffs. At other seasons, a more complex combination of processes governs the SSS IAV.

## 5. Summary and Discussion

### 5.1. Summary

The BoB intense near-surface haline stratification is believed to exert a strong control on upper ocean mixing and surface temperature, and thus on the climate of the neighboring countries [Shenoi *et al.*, 2002]. Several studies have already investigated BoB seasonal SSS variations and their driving mechanisms, using both observations and models [Rao and Sivakumar, 2003; Shetye, 1993; Shetye *et al.*, 1991, 1996; Vinayachandran *et al.*, 2002; Vinayachandran and Kurian, 2007; Benshila *et al.*, 2014; Akhil *et al.*, 2014; Chaitanya *et al.*, 2014]. Due to the scarcity of available in situ observations, however, little is known about the BoB SSS interannual variability. The BoB SSS observing system and modeling platforms have clearly improved over the

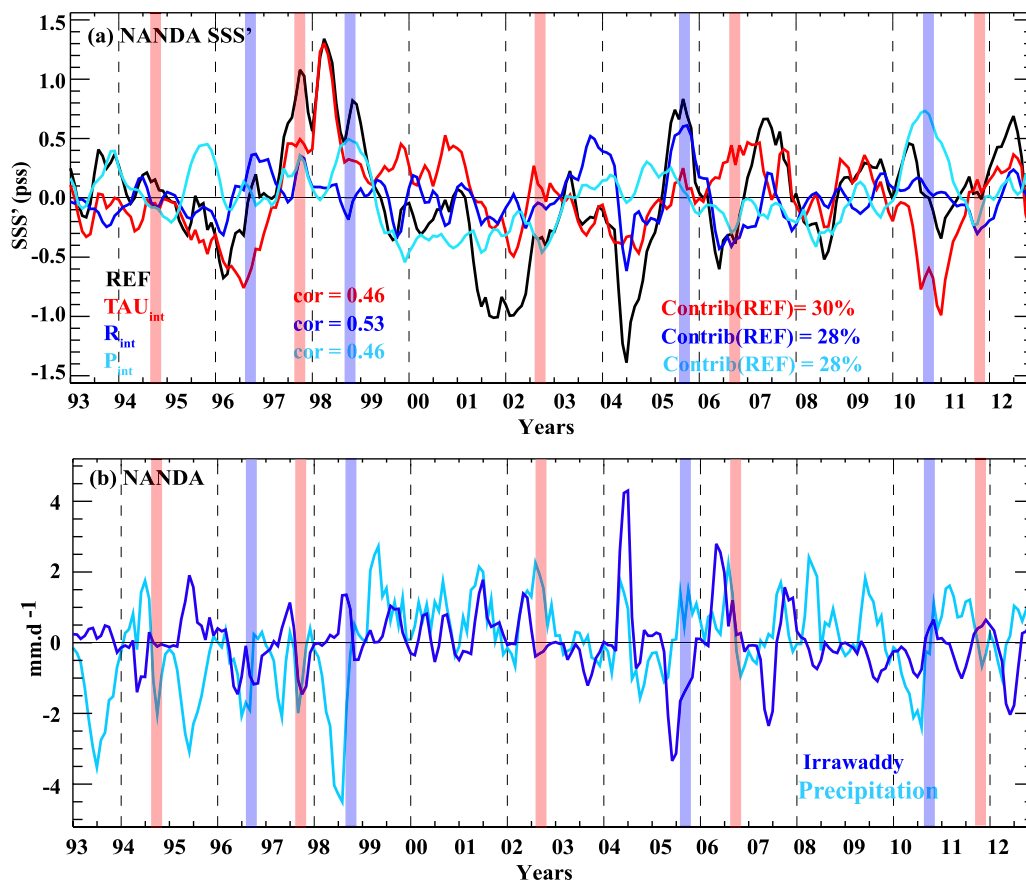


**Figure 13.** (a) Time series of monthly average NANDA SSS interannual anomalies in REF (black),  $Tau_{int}$  (red),  $P_{int}$  (light blue), and  $R_{int}$  (deep blue) experiments. The correlation and relative contributions of the interannual variability of each forcing to SSS'(REF) are indicated on Figure 13a, along with positive (red-shading) and negative (blue-shading) IOD events. (b) Time series of interannual precipitation (light blue) and Irrawaddy (deep blue) runoff anomalies (converted into  $mm \cdot d^{-1}$  through dividing by the area of the NANDA box). The shading indicates positive (red) and negative (blue) IOD events.

past few years. The aim of the current study is thus to use a series of simulations validated against available observations to describe SSS interannual variability in the BoB and understand its driving mechanisms.

The observational data set consists of a blended product of all available BoB in situ SSS observations during the 2006–2012 period. We force an eddy-permitting ( $1/4^\circ$ ) regional ocean model with realistic interannual air-sea fluxes, an altimeter-derived interannual runoff for major rivers and no relaxation toward climatological observed SSS. We also perform sensitivity experiments where only interannual variations of either wind stress, precipitation, or river runoffs are specified, other forcings being set to their seasonal climatology. Modeled SSS interannual anomalies from the reference experiment agree qualitatively well with observations. Maximum SSS interannual variations occur around the rim of the Bay right after the monsoon, with a minimum variability in the central part of the basin, in both the model and observations. The modeled and observed SSS interannual anomalies are in good agreement in the two regions of strongest variability, i.e., the northern BoB and along the east coast of India (correlations between 0.6 and 0.7). Interannual SSS anomalies cannot be validated in the third region of strong variability, i.e., the Andaman Sea, due to the lack of in situ data. SSS interannual anomalies in the southern Andaman Sea exhibit opposite fluctuations to those along the East Indian coastline, while the northern BoB SSS variability is more independent from that in other regions.

In the northern BoB, SSS interannual variations are largest in fall and winter. Northern BoB SSS anomalies after the summer monsoon ( $\sim 1$  pss amplitude) are largely driven by interannual variations of the GB river runoff ( $-0.76$  correlation), with interannual variations of precipitations playing a minor role. These SSS anomalies are moderately correlated with ENSO ( $\sim 0.4$ ), probably because of the influence of this climate

mode on the rainfall over the catchment basin of the GB [Vecchi and Harrison, 2004]. In SON, those SSS anomalies modulate the vertical salinity gradient at the bottom of the mixed layer, a surface freshening being associated with a sharper halocline. This sharper halocline then intensifies the surface saltening by vertical mixing, thus providing a regulating mechanism that damps the SSS anomalies generated by GB variations.

SSS interannual anomalies are also large along the western boundary and in the southern Andaman Sea right after the monsoon and remotely controlled by the IOD-related wind anomalies. Positive IOD events induce easterly wind anomalies in the equatorial region and anticyclonic anomalies in the Bay of Bengal. Those signals both force coastal upwelling Kelvin waves that propagate anticlockwise around the rim of the BoB. The related negative sea level anomalies along the east coast of India weaken the EICC, hence limiting the seasonal southward advection of fresh water from the northern part of the Bay [Chaitanya *et al.*, 2014; Akhil *et al.*, 2014] and resulting in a positive SSS anomaly of the order of 1 pss there. Conversely, during a negative IOD event, downwelling Kelvin waves induce an acceleration of EICC, favoring the southward advection of the fresh plume. Similarly to what happens in the NBoB region, SSS anomalies along the east coast of India are then dissipated through the effect of vertical mixing. In the Andaman Sea, positive IOD events drive southward current anomalies that anomalously advect fresh waters from the northern part of the sub-basin into the southern Andaman Sea. Winter climatological northwestward currents in the southern BoB then advect these fresh SSS' from the Andaman Sea to the central BoB, resulting in the freshening decay in the SANDA region. While GB runoff interannual variations dominate SSS IAV close to the river mouth, wind interannual anomalies play a strong role in spreading these anomalies over the rest of the NBoB box.

Finally, interannual SSS anomalies in the northern Andaman Sea are maximum during the monsoon and partly related to interannual Irrawady runoffs variations ( $-0.74$  correlation). The balance is more complex at other seasons, when a mix of wind, runoff, and precipitation variations influences SSS interannual variability.

## 5.2. Discussion

Only a handful of studies did specifically address BoB interannual SSS variability [Vinayachandran and Nanjudiah, 2009; Durand *et al.*, 2011; Chaitanya *et al.*, 2014; Pant *et al.*, 2015]. In line with the present results, all these studies acknowledged that largest SSS interannual variations occur in the northern part of the Bay, shortly after the monsoon and are predominantly driven by interannual variability of the freshwater flux. There is however no consensus on the respective contribution of oceanic precipitations and GB river runoffs to SSS fluctuations in this region. The two observational analyses that address this issue using simple mixed layer salt budgets reach different conclusions: Pant *et al.* [2015] suggest that most of these fluctuations are driven by oceanic precipitations over the 2006–2013 period, but Chaitanya *et al.* [2014] pointed toward a combined and rather independent contribution from oceanic precipitations and river runoffs over the 2009–2014 period. Our modeling results indicate that interannual GB runoff fluctuations dominate the SSS variations in the northern BoB over the last two decades, the impact of precipitations being nearly negligible. Other modeling studies [Vinayachandran and Nanjudiah, 2009; Durand *et al.*, 2011] also underline the importance of interannual GB runoffs fluctuations on SSS interannual variability in the northern Bay, although they did not precisely quantify their contribution. A careful examination however partly reconciles the apparent contradiction with Chaitanya *et al.* [2014] results: they indeed show that the strong saltening event from summer 2009 to fall 2010 can be almost entirely attributed to GB fluctuations (their Figures 7 and 8), in line with our results (our Figure 10). In contrast, they attributed the freshening from fall 2010 to winter 2012 to a combination of anomalous precipitations, runoffs, and horizontal advection: during this period, our model results also show that, in addition to the influence GB fluctuations, both precipitation and wind stress variations significantly contribute to SSS variations (Figure 10). In contrast, it is not straightforward to compare our results with those of Pant *et al.* [2015] as they did not clearly separate out the contribution of local precipitations and runoffs on the NBoB SSS variability. In any case, the different estimated contributions of precipitations and runoffs between these studies and the present one may arise from their limited temporal coverage compared to the present study covering almost two decades.

All the studies dealing with the processes driving interannual SSS variations in the BoB also point toward an influence of ocean dynamics in fall and winter. Durand *et al.* [2011] show that anomalous EICC variations modulate the horizontal advection of fresh waters from the northern BoB and hence play a strong role in

driving the interannual SSS variability along the eastern coast of India, but could not identify the mechanisms driving these deviations of EICC magnitude. Both *Vinayachandran and Nanjudiah* [2009] and *Pant et al.* [2015] concluded that horizontal advection is the dominant contributor to the tendency term during the winter season. Our results clearly demonstrate that the eastern Indian coast is the second largest region of SSS interannual variability in the BoB with maximum signals during the fall and winter season. In line with *Durand et al.* [2011], our mixed layer salinity budget analysis shows that the fall variability in that region is driven by interannual variations of the EICC, which modulate the amount of fresh water transported from the northern head of the Bay. Our results further demonstrate a strong influence of the vertical processes during winter in eroding these SSS anomalies along the coast. In line with *Pant et al.* [2015], our results also indicate that horizontal advection processes largely drive SSS variability in the southern part of the BoB. We however show that these anomalies arise from anomalous advection of freshwater from the Andaman Sea rather than from the northern part of the Bay as initially suggested by *Pant et al.* [2015].

Several studies have discussed the influence of IOD events on BoB SSS [*Vinayachandran and Nanjudiah*, 2009; *Chaitanya et al.*, 2014; *Pant et al.*, 2015]. As suggested by *Vinayachandran and Nanjudiah* [2009] and *Pant et al.* [2015], we demonstrate that IOD events are responsible for interannual salinity variations along the eastern coast of India through their remote impact on the EICC. Our results also attribute the SSS interannual variability in the southern part of the Bay to anomalies of horizontal advective processes related to this climate mode, in line with other studies [*Thompson et al.*, 2006; *Vinayachandran and Nanjudiah*, 2009; *Grunseich et al.*, 2011; *Durand et al.*, 2013; *Pant et al.*, 2015]. On the other hand, while *Pant et al.* [2015] attribute the NBoB summer SSS anomalies in the northern BoB to IOD-related precipitation, we find that anomalies are unrelated with IOD events in this region ( $-0.18$  Correlation with DMI index) but largely result from GB interannual fluctuations ( $-0.76$  correlation). The SSS variability in NBoB is moderately correlated with ENSO ( $-0.43$  correlation), as a result of ENSO influence on the rainfall over the Ganges-Mahanadi watershed [*Vecchi and Harrison*, 2004]. It may again well be that this mismatch between our study and *Pant et al.* [2015] arises from the short period over which their analysis is performed, which does not allow to clearly separate ENSO from the IOD, while these two climate modes often cooccur [*Aparna et al.* 2012].

The rather good agreement between the model and observed SSS interannual variations in the NBoB and WBoB gives us confidence in the mechanisms responsible for the SSS variations diagnosed from our model. However, an obvious caveat of the present model configuration is to underestimate the amplitude of the SSS variations in the WBoB (Figure 3b). There are several possible reasons for that. First, the comparisons between model and observations in *Akhil et al.* [2014] suggest that the model postmonsoon SSS may be overestimated in the northern BoB, hence resulting in an underestimated meridional advection along the east coast of India. A first way to improve the SSS interannual variations in the model would hence be to improve the SSS mean state, for example through a flux correction approach. As shown by *Benshila et al.* [2014], the  $\sim 25$  km resolution of our model also does not allow to fully simulate the intense and narrow structure of the EICC, which would also tend to result in underestimated meridional advection there. The western rim of the BoB is an area of intense eddy activity [*Durand et al.*, 2009]. Our model is eddy-permitting, but not really eddy-resolving, and does not permit assessing the effect of the oceanic mesoscale circulation on the coastal freshwater strip, which is probably strong [e.g., *Hareesh Kumar et al.*, 2013]. Refining the model resolution may therefore also be a way to further improve the realism of our simulation. Increasing the horizontal resolution may improve the representation of the EICC and offshore freshwater export from this coastal freshwater strip while increasing the vertical resolution in the upper layers (from 6 to 1 m) may also improve the representation of vertical mixing in occasionally very sharp near-surface salinity stratification in the BoB [*Vinayachandran and Kurian*, 2007].

Although our simulation indicates that the Andaman Sea is the third largest region of SSS interannual variations in the BoB, it is difficult to assess the realism of our simulation in this region due to the dearth of in situ observations. The shallow bathymetry has so far prevented the deployment of Argo profilers in this region. Argo profilers with shallower than usual parking depth, moorings, dedicated oceanic cruises but also remotely-sensed SSS estimation from Aquarius, SMOS and SMAP (Soil Moisture Active and Passive, NASA's latest satellite successfully launched on 29th January 2015, see <http://smap.jpl.nasa.gov/>) may however provide valuable information on interannual SSS fluctuations in this region in the near future. In this paper, we did not discuss the interannual SSS variations in the central part of the Bay, because these signals are far weaker than along the rim of the Bay (Figure 4) and because our model does not perform well in

reproducing the SSS variations there (not shown). An improved simulation of modeled SSS in this region is therefore a prerequisite before studying the mechanisms at stake in driving these weaker SSS interannual variations in the central BoB.

#### Acknowledgments

The authors thank IFCPAR (Indo French Centre for Promotion of Advanced Research), New Delhi for funding of the proposal 4907-1 and LEFE/EC2CO program for funding of the proposal AO2015-873251. We also acknowledge the financial support from CNES (Centre National d'Etudes Spatiales), the French Space Agency. We thank IRD (Institut de Recherche pour le Développement) for the financial support for the Indo-French collaboration on Indian Ocean research. In situ SSS samples are collected under support from Ministry of Earth Sciences (Government of India, [odis.incois.gov.in](http://odis.incois.gov.in)). We are thankful to the ARGO ([ftp.ifremer.fr/ifremer/argo](http://ftp.ifremer.fr/ifremer/argo)) and RAMA projects (<http://www.pmel.noaa.gov/tao/disdeld/disdeld-rama.html>), the NIOT staff ([odis.incois.gov.in](http://odis.incois.gov.in)), and the French SSS Observation Service ([www.legos.obs-mip.fr/observations/sss](http://www.legos.obs-mip.fr/observations/sss)) for the OMNI moorings and thermosalinograph data delivery. We thank Bruno Blanke and Vincent Echevin for their valuable comments on an earlier version of this manuscript. Clément de Boyer Montégut is supported by the European Union via the seventh Framework Programme (INCO\_LAB GA295092 INDO-MARECLIM).

#### References

- Akhil, V. P., F. Durand, M. Lengaigne, J. Vialard, M. G. Keethi, V. V. Gopalakrishna, C. Deltel, F. Papa, and C. de Boyer Montégut (2014), A modeling study of the processes of surface salinity seasonal cycle in the Bay of Bengal, *J. Geophys. Res. Oceans*, *116*, 3926–3947, doi: 10.1002/2013JC009632.
- Akhil, V. P., M. Lengaigne, F. Durand, J. Vialard, A. V. S. Chaitanya, M. G. Keethi, V. V. Gopalakrishna, J. Boutin, and C. de Boyer Montégut (2016), Assessment of seasonal and year-to-year surface salinity signals retrieved from SMOS and Aquarius missions in the Bay of Bengal, *Int. J. Remote Sens.*, *37*(5), 1089–1114, doi:10.1080/01431161.2016.1145362.
- Alory, G., et al. (2015), The French contribution to the voluntary observing ships network of sea surface salinity, *Deep Sea Res., Part I*, *105*, 1–18, doi:10.1016/j.dsr.2015.08.005.
- Aparna, S. G., J. P. McCreary, D. Shankar, and P. N. Vinayachandran (2012), Signatures of Indian Ocean Dipole and El Niño–Southern Oscillation events in sea level variations in the Bay of Bengal, *J. Geophys. Res.*, *117*, C10012, doi:10.1029/2012JC008055.
- Benshila, R., F. Durand, S. Masson, R. Bourdalle-Badie, C. de Boyer Montégut, F. Papa, and G. Madec (2014) The upper Bay of Bengal salinity structure in a high-resolution model, *Ocean Modell.*, *74*, 36–52.
- Blanke, B., and P. Delecluse (1993), Low frequency variability of the tropical Atlantic Ocean simulated by a general circulation model with mixed layer physics, *J. Phys. Oceanogr.*, *23*, 1363–1388.
- Brodeau et al., (2012), An ERA40-based atmospheric forcing for global ocean circulation models, *Ocean Modell.*, *31*(34), 88–104.
- Chaitanya, V. S., M. Lengaigne, J. Vialard, V. V. Gopalakrishna, F. Durand, C. KranthiKumar, S. Amritash, V. Suneel, F. Papa, and M. Ravichandran (2014), Salinity Measurements Collected by Fishermen Reveal a “River in the Sea” Flowing Along the Eastern Coast of India, *Bull. Am. Meteorol. Soc.*, *95*, 1897–1908, doi:10.1175/BAMS-D-12-00243.1.
- Chaitanya, A. V. S., F. Durand, S. Mathew, V. V. Gopalakrishna, F. Papa, M. Lengaigne, J. Vialard, C. Krantikumar, and R. Venkatesan (2014), Observed year-to-year sea surface salinity variability in the Bay of Bengal during the period 2009–2014, *Ocean Dyn.*, doi:10.1007/s10236-014-0802-x.
- Chatterjee, A., et al. (2012), A new atlas of temperature and salinity for the north Indian Ocean, *J. Earth Syst. Sci.*, *121*(3), 559–593, doi: 10.1007/s12040-012-0191-9.
- Dai, A., and K. E. Trenberth (2002), Estimates of freshwater discharge from continents: Latitudinal and seasonal variations, *J. Hydrometeorol.*, *3*(6), 660–687.
- de Boyer Montégut, C., J. Mignot, A. Lazar, and S. Cravatte (2007), Control of salinity on the mixed layer depth in the world ocean. Part I: General description, *J. Geophys. Res.*, *112*, C06011, doi:10.1029/2006JC003953.
- Dee, D. P., et al. (2011), The ERA-interim reanalysis: Configuration and performance of the data assimilation system, *Q. J. R. Meteorol. Soc.*, *137*, 553–597, doi:10.1002/qj.828.
- Drakkar Group (2007), Eddy-permitting ocean circulation hindcasts of past decades, *CLIVAR Exchanges*, *42* 12(3), 8–10.
- Durand, F., D. Shankar, C. de Boyer Montégut, S. S. C. Shenoi, B. Blanke, and G. Madec (2007), Modeling the barrier-layer formation in the Southeastern Arabian Sea, *J. Clim.*, *20*, 2109–2120, doi:10.1175/JCLI4112.1.
- Durand, F., F. Papa, A. Rahman, and S. K. Bala (2011) Impact of Ganges-Brahmaputra interannual discharge variations on Bay of Bengal salinity, *J. Earth Syst. Sci.*, *120*(5), 859–872, doi:10.1007/s12040-011-0118-x.
- Durand, F., G. Alory, R. Dussin, and N. Reul (2013), SMOS reveals the signature of Indian Ocean Dipole events, *Ocean Dyn.*, *63*(11–12), 1203–1212.
- Dussin, R., B. Barnier, and L. Brodeau (2014), Atmospheric forcing data sets to drive eddy-resolving global ocean general circulation models, Abstract 1716 presented at EGU General Assembly Conference Abstracts, vol. 16, p.1716, EGU, Vienna, Austria.
- Furuichi, T., Z. Win, and R. J. Wasson (2009), Discharge and suspended sediment transport in the Ayeyarwady River, Myanmar: Centennial and decadal changes, *Hydrol. Processes*, *23*, 1631–1641, doi:10.1002/hyp.7295.
- Gadgil, S. (2003) The Indian Monsoon and its variability, *Annu. Rev. Earth Planet. Sci.*, *31*, 429–467.
- Gadgil, S., P. V. Joseph, and N. V. Joshi (1984), Ocean–atmosphere coupling over monsoon regions, *Nature*, *312*, 141–143.
- Girishkumar, M. S., M. Ravichandran, and M. J. McPhaden (2013), Temperature inversions and their influence on the mixed layer heat budget during the winters of 2006–2007 and 2007–2008 in the Bay of Bengal, *J. Geophys. Res. Oceans.*, *118*, 2426–2437, doi: 10.1002/jgrc.20192.
- Grunseich, G., B. Subrahmanyam, V. S. N. Murty, and B. S. Giese (2011), Sea surface salinity variability during the Indian Ocean Dipole and ENSO events in the tropical Indian Ocean, *J. Geophys. Res.*, *116*, C11013, doi:10.1029/2011JC007456.
- Han, W., and P. J. Webster (2002), Forcing mechanisms of sea-level interannual variability in the Bay of Bengal, *J. Phys. Oceanogr.*, *32*, 216–239.
- Han, W., J. P. McCreary, and K. E. Kohler (2001), Influence of precipitation minus evaporation and Bay of Bengal rivers on dynamics, thermodynamics, and mixed layer physics in the upper Indian Ocean, *J. Geophys. Res.*, *106*, 6895–6916.
- Hareesh Kumar, P. V., B. Matthew, M. R. Ramesh Kumar, A. R. Rao, P. S. V. Jagadeesh, K. G. Radhakrishnan, and T. N. Shyni (2013), ‘Thermohaline front’ off the east coast of India and its generating mechanism, *Ocean Dyn.*, *63*, 1175–1180, doi:10.1007/s10236-013-0652-y.
- Huffman, G., et al. (1997), The global precipitation climatology project (GPCP) combined precipitation data set, *Bull. Am. Meteorol. Soc.*, *78*, 5–20.
- Izumo, T., M. Lengaigne, J. Vialard, J.-J. Luo, T. Yamagata, and G. Madec (2014), Influence of Indian Ocean Dipole and Pacific recharge on following year’s El Niño: Interdecadal robustness, *Clim. Dyn.*, *42*(1–2), 291–310.
- Jensen, T. G. (2001), Arabian Sea and Bay of Bengal exchange of salt and tracers in an ocean model, *Geophys. Res. Lett.*, *28*, 3967–3970.
- Jensen, T. G. (2007), Wind-driven response of the northern Indian Ocean to climate extremes, *J. Clim.*, *20*, 2978–2993, doi:10.1175/JCLI4150.1
- Keerthi, M. G., M. Lengaigne, J. Vialard, C. de Boyer Montégut, and P. M. Muraleedharan (2013), Interannual variability of the Tropical Indian Ocean mixed layer depth, *Clim. Dyn.*, *40*, 743–759.
- Keerthi, M. G., M. Lengaigne, K. Drushka, J. Vialard, C. de Boyer Montégut, S. Pous, M. Levy, and P. M. Muraleedharan (2016), Intraseasonal variability of mixed layer depth in the tropical Indian, *Clim. Dyn.*, *46*(7–8), 2633–2655, doi:10.1007/s00382-015-2721-z.

- Klein, S. A., B. J. Soden, and N. C. Lau (1999), Remote sea surface temperature variations during ENSO: Evidence for a tropical atmospheric bridge, *J. Clim.*, *12*, 917–932.
- Locarnini, R. A., A. V. Mishonov, J. I. Antonov, T. P. Boyer, H. E. Garcia, O. K. Baranova, M. M. Zweng, and D. R. Johnson (2010), World Ocean Atlas, 2009, vol. 1, in *NOAA Atlas NESDIS 68*, edited by T. S. Levitus, U.S. Gov. Print. Off., Washington, D. C.
- Lukas, R. B., and E. J. Lindstrom (1991), The mixed layer of the western equatorial Pacific Ocean, *J. Geophys. Res.*, *96*, 3343–3357.
- Madec, G. (2008), NEMO ocean engine, Note Pôle Modél. 27, Inst. Pierre-Simon Laplace, Paris.
- Marchesiello, P., J. C. McWilliams, and A. F. Shchepetkin (2001), Open boundary conditions for long-term integration of regional ocean models, *Ocean Modell.*, *3*, 1–20.
- McCreary, J. P., W. Han, D. Shankar, and S. R. Shetye (1996), Dynamics of the East India Coastal Current: 2. Numerical solutions, *J. Geophys. Res.*, *101*, 13,993–14,010, doi:10.1029/96JC00560.
- McPhaden, M. J., et al. (2009), RAMA: The research moored array for African-Asian-Australian monsoon analysis and prediction, *Bull. Am. Meteorol. Soc.*, *90*, 459–480.
- Mignot, J., C. de Boyer Montégut, A. Lazar, and S. Cravatte (2007) Control of salinity on the mixed layer depth in the world ocean: 2. Tropical areas, *J. Geophys. Res.*, *112*, C10010, doi:10.1029/2006JC003954.
- Mujumdar, M., B. Preethi, T. P. Sabin, K. Ashok, S. Saeed, D. S. Pai, and R. Krishnan (2012), The Asian summermonsoon response to the LaNiña event of 2010, *Meteorol. Appl.*, *19*, 216–225.
- Neetu, S., M. Lengaigne, E. M. Vincent, J. Vialard, G. Madec, G. Samson, M. R. Ramesh Kumar, and F. Durand (2012), Influence of upper-ocean stratification on tropical cyclone-induced surface cooling in the Bay of Bengal, *J. Geophys. Res.*, *117*, C12020, doi:10.1029/2012JC008433.
- Nidheesh, A. G., M. Lengaigne, J. Vialard, A. S. Unnikrishnan, and H. Dayan (2012), Decadal and long-term sea level variability in the tropical Indo-Pacific Ocean, *Clim. Dyn.*, *41*, 381–402.
- Nisha, K., M. Lengaigne, V. V. Gopalakrishna, J. Vialard, S. Pous, A. C. Peter, F. Durand, and S. Naik (2013), Processes of summer intraseasonal sea surface temperature variability along the coasts of India, *Ocean Dyn.*, *63*, 329–346.
- Pant, V., M. S. Girishkumar, T. V. S. Udaya Bhaskar, M. Ravichandran, F. Papa, and V. P. Thangaprakash (2015), Observed interannual variability of near-surface salinity in the Bay of Bengal, *J. Geophys. Res. Oceans*, *120*, 3315–3329, doi:10.1002/2014JC010340.
- Papa, F., F. Durand, A. Rahman, S. K. Bala, and W. B. Rossow (2010), Satellite altimeter-derived monthly discharge of the Ganga-Brahmaputra River and its seasonal to interannual variations from 1993 to 2008, *J. Geophys. Res.*, *115*, C12013, doi:10.1029/2009JC006075.
- Papa, F., S. K. Bala, R. K. Pandey, F. Durand, V. V. Gopalakrishna, A. Rahman, and W. B. Rossow (2012), Ganga-Brahmaputra river discharge from Jason-2 radar altimetry: An update to the long-term satellite-derived estimates of continental freshwater forcing flux into the Bay of Bengal, *J. Geophys. Res.*, *117*, C11021, doi:10.1029/2012JC008158.
- Praveen Kumar, B., J. Vialard, M. Lengaigne, V. S. N. Murty, and M. J. McPhaden (2012), TropFlux: Air-sea fluxes for the global tropical oceans—description and evaluation against observations, *Clim. Dyn.*, *38*, 1521–1543.
- Praveen Kumar, B., J. Vialard, M. Lengaigne, V. S. N. Murty, G. R. Foltz, M. J. McPhaden, S. Pous, and C. de Boyer Montégut (2014), Processes of interannual mixed layer temperature variability in the thermocline ridge of the Indian Ocean, *Clim. Dyn.*, *43*, 2377, doi:10.1007/s00382-014-2059-y.
- Rao, R. R., and R. Sivakumar (2003), Seasonal variability of sea surface salinity and salt budget of the mixed layer of the north Indian Ocean, *J. Geophys. Res.*, *108*(C1), 3009, doi:10.1029/2001JC00907.
- Rao, S. A., S. K. Behera, Y. Masumoto, and T. Yamagata (2002), Interannual subsurface variability in the tropical Indian Ocean with a special emphasis on the Indian Ocean Dipole, *Deep Sea Res., Part II*, *49*(7–8), 1549–1572, doi:10.1016/S0967-0645(01)00158-8.
- Roemmich, D., et al. (2009), The Argo Program: Observing the global ocean with profiling floats, *Oceanography*, *22*(2), 34–43, doi:10.5670/oceanog.2009.36.
- Saji, N. H., B. N. Goswami, P. N. Vinayachandran, and T. Yamagata (1999), A dipole mode in the tropical Indian Ocean, *Nature*, *401*(6751), 360–363.
- Saji, N. H., and T. Yamagata (2003), Structure of SST and surface wind variability during Indian Ocean Dipole Mode events: COADS observations, *J. Clim.*, *16*, 2735–2751.
- Sengupta, D., G. N. Bharath Raj, and S. S. C. Shenoi (2006), Surface freshwater from Bay of Bengal runoff and Indonesian throughflow in the tropical Indian Ocean, *Geophys. Res. Lett.*, *33*, L22609, doi:10.1029/2006GL027573.
- Sengupta, D., R. G. Bharath, and D. S. Anitha (2008), Cyclone-induced mixing does not cool SST in the post-monsoon north Bay of Bengal, *Atmos. Sci. Lett.*, *9*, 1–6, doi:10.1002/asl.162.
- Shankar, D. (1998), Low-frequency variability of sea level along the coast of India, PhD thesis, 207 pp., Goa Univ., Goa, India. [Available at <http://hdl.handle.net/2264/24>.]
- Shankar, D., J. P. McCreary, W. Han, and S. R. Shetye (1996), Dynamics of the East India Coastal Current 1. Analytic solutions forced by interior Ekman pumping and local alongshore winds, *J. Geophys. Res.*, *101*, 13,975–13,991, doi:10.1029/96JC00559.
- Shenoi, S. S. C., D. Shankar, and S. R. Shetye (2002), Difference in heat budgets of the near-surface Arabian Sea and Bay of Bengal: Implications for the summer monsoon, *J. Geophys. Res.*, *107*(C6), 3052, doi:10.1029/2000JC000679.
- Shetye, S. R. (1993), The movement and implications of the Ganges-Brahmaputra runoff on entering the Bay of Bengal, *Curr. Sci.*, *64*(1), 32–38.
- Shetye, S. R., S. S. C. Shenoi, A. D. Gouveia, G. S. Michael, D. Sundar, and G. Nampoothiri (1991), Wind-driven coastal upwelling along the western boundary of the Bay of Bengal during the southwest monsoon, *Cont. Shelf Res.*, *11*, 1397–1408.
- Shetye, S. R., A. D. Gouveia, D. Shankar, G. S. Michael, and G. Nampoothiri (1996), Hydrography and circulation of the western Bay of Bengal during the Northeast Monsoon, *J. Geophys. Res.*, *101*, 14,011–14,025.
- Singh, O. P. (2002), Interannual variability and predictability of sea level along the Indian Coast, *Theor. Appl. Climatol.*, *72*, 11–28.
- Srinivas, K., P. K. D. Kumar, and C. Revichandran (2005), ENSO signature in the sea level along the coastline of the Indian subcontinent, *Indian J. Mar. Sci.*, *34*, 225–236.
- Thadathil, P., P. M. Muraleedharan, R. R. Rao, Y. K. Somayajulu, G. V. Reddy, and C. Revichandran (2007), Observed seasonal variability of barrier layer in the Bay of Bengal, *J. Geophys. Res.*, *112*, C02009, doi:10.1029/2006JC003651.
- Thompson, B., C. Gnanaseelan, and P. S. Salvekar (2006), Variability in the Indian Ocean circulation and salinity and its impact on SST anomalies during dipole events, *J. Mar. Res.*, *64*, 853–880.
- Uppala, S. M., et al. (2005), The ERA-40 re-analysis, *Q. J. R. Meteorol. Soc.*, *131*, 2961–3012, doi:10.1256/qj.04.176.
- Vecchi, G. A., and D. E. Harrison (2004), Interannual Indian rainfall variability and Indian Ocean sea surface temperature anomalies, Earth climate: The ocean atmosphere interaction, *AGU, Geophys. Monogr.*, *147*, (Eds.) C. Wang, 247–260.
- Venkatesan, R., M. Arul Muthiah, K. Ramesh, S. Ramasundaram, R. Sundar, and M. A. Atmanand (2013), Satellite communication systems for ocean observational platforms: Societal importance and challenges, *J. Ocean Technol.*, *8*(3), 47–73.

- Vialard, J., K. Drushka, H. Bellenger, M. Lengaigne, S. Pous, and J. P. Duvel (2013), Understanding Madden-Julian-Induced sea surface temperature variations in the North Western Australian Basin, *Clim. Dyn.*, *41*, 3203–3218.
- Vinayachandran, P. N., and J. Kurian (2007), Hydrographic observations and model simulation of the Bay of Bengal freshwater plume, *Deep Sea Res., Part I*, *54*, 471–486.
- Vinayachandran, P. N., V. S. N. Murty, and V. Ramesh Babu (2002), Observations of barrier layer formation in the Bay of Bengal during summer monsoon, *J. Geophys. Res.*, *107*(C12), doi:10.1029/2001JC000831.
- Vinayachandran, P. N., and R. S. Nanjundiah (2009), Indian Ocean sea surface salinity variations in a coupled model, *Clim Dyn.*, *33*, 245–263, doi:10.1007/s00382-008-0511-6.
- Vinayachandran, P. N., C. P. Neema, S. Mathew, and R. Remya (2012), Mechanisms of summer intraseasonal sea surface temperature oscillations in the Bay of Bengal, *J. Geophys. Res.*, *117*, C01005, doi:10.1029/2011JC007433.
- Vinayachandran, P. N., D. Shankar, S. Vernekar, K. K. Sandeep, P. Amol, C. P. Neema, and A. Chatterjee (2013), A summer monsoon pump to keep the Bay of Bengal salty, *Geophys. Res. Lett.*, *40*, 1777–1782, doi:10.1002/grl.50274.
- Webster, P. J., A. M. Moore, J. P. Loschnigg, and R. R. Leben (1999), Coupled ocean-atmosphere dynamics in the Indian Ocean during 1997–98, *Nature*, *401*(6751), 356–60, doi:10.1038/43848.
- Xie, S. P., J. Hafner, H. Tokinaga, Y. Du, T. Sampe, and H. G. Hu KaiMing (2009), Indian Ocean capacitor effect on Indo-western Pacific climate during the summer following El Niño, *J. Clim.*, *22*(3), 730–747, doi:10.1175/2008JCLI2544.1.
- Yamagata, T., S. K. Behera, J.-J. Luo, S. Masson, M. R. Jury, and S. A. Rao (2004), The coupled ocean-atmosphere variability in the tropical Indian Ocean, in *Earth's Climate: The Ocean-Atmosphere Interaction*, *Geophys. Monogr.*, vol. 147, edited by C. Wang, S. P. Xie and J. A. Carton, pp. 189–211, AGU, Washington, D. C., doi:10.1029/147GM12.
- Zhang, Y. C., W. B. Rossow, A. A. Lacis, V. Oinas, and M. I. Mishchenko (2004), Calculation of radiative flux profiles from the surface to top-of-atmosphere based on ISCCP and other global datasets: Refinements of the radiative transfer model and the input data, *J. Geophys. Res.*, *27*, D19105, doi:10.1029/2003JD004457.